ACS Catalysis

Research Article

pubs.acs.org/acscatalysis

Computing Free Energy Landscapes: Application to Ni-based Electrocatalysts with Pendant Amines for H_2 Production and Oxidation

Shentan Chen, Ming-Hsun Ho, R. Morris Bullock, Daniel L. DuBois, Michel Dupuis, Roger Rousseau,* and Simone Raugei*

Center for Molecular Electrocatalysis, Pacific Northwest National Laboratory, P.O. Box 999, K1-83, Richland, Washington 99352, United States

Ⓢ *Supporting Information*

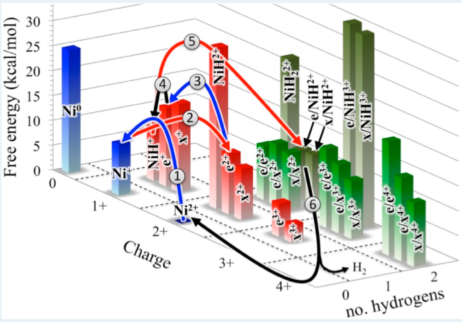

ABSTRACT: A general strategy is reported for the computational exploration of catalytic pathways of molecular catalysts. Our results are based on a set of linear free energy relationships derived from extensive electronic structure calculations that permit predicting the thermodynamics of intermediates, with accuracy comparable to experimental data. The approach is exemplified with the catalytic oxidation and production of H_2 by $[Ni(diphosphine)_2]^{2+}$ electrocatalysts with pendant amines incorporated in the second coordination sphere of the metal center. The analysis focuses upon prediction of thermodynamic properties including reduction potentials, hydride donor abilities, and pK_a values of both the protonated Ni center and the pendant amine. It is shown that all of these chemical properties can be estimated from the knowledge of only the two redox potentials for the Ni(II)/Ni(I) and Ni(I)/Ni(0) couples of the nonprotonated complex, and the pK_a of the parent primary aminium ion. These three quantities are easily accessible either experimentally or theoretically. The proposed correlations reveal intimate details about the nature of the catalytic mechanism and its dependence on chemical structure and thermodynamic conditions such as applied external voltage and species concentration. This computational methodology is applied to the exploration of possible catalytic pathways, identifying low and high-energy intermediates and, consequently, possibly avoiding bottlenecks associated with undesirable intermediates in the catalytic reactions. We discuss how to optimize some of the critical reaction steps to favor catalytically more efficient intermediates. The results of this study highlight the substantial interplay between the various parameters characterizing the catalytic activity, and form the basis needed to optimize the performance of this class of catalysts.

KEYWORDS: *molecular electrocatalysis, thermodynamics, Ni complexes, computational chemistry, hydrogen oxidation and production, catalyst optimization*

1. INTRODUCTION

Development of electrocatalysts based on inexpensive, abundant metals[1,2] for rapid and efficient interconversion between electrical energy and fuels is critical for renewable energy utilization systems.[3−5] One general approach to improve the efficiency of existing catalysts and design new ones is to eliminate low and high-energy intermediates and, consequently, reduce the barriers associated with these intermediates in the catalytic reactions. This thermochemical approach to catalyst design relies on the knowledge of the relative free energies of potential intermediates in the catalytic cycle. This approach has been successfully applied to the development of efficient Co-based catalysts for CO_2 reduction[6] and Ni-based molecular electrocatalysts for hydrogen oxidation, hydrogen production, and formate oxidation.[7,8] It has also been applied to stoichiometric reactions such as hydride transfer from rhodium and cobalt hydrides to boron compounds to form borohydrides,[9−11] and from nickel and platinum hydrides to metal carbonyl complexes to generate formyl complexes.[12] All of these catalytic and stoichiometric reactions are potentially important for electrical energy storage and conversion technologies. In the current study we use a combination of ab initio electronic structure calculations and simple quantitative structure activity relationships to quantify and systematize this approach and demonstrate how in doing so this leads to new insights into catalyst optimization. A Ni-based family of electrocatalysts for H_2 production and oxidation for which very extensive thermodynamic information has been compiled will serve as a focus of the current study.[7,8,13−21]

Previously we reported a theoretical model capable of generating free energy relationships based only on the knowledge of two redox potentials for a series of Ni(diphosphine)$_2$ complexes that can promote the cleavage of H_2.[22] The general structure of this class of complexes is shown in Figure 1a, which we will refer to as P_2 systems. However,

Received: November 22, 2013
Published: November 27, 2013

dx.doi.org/10.1021/cs401104w | *ACS Catal.* 2014, 4, 229−242

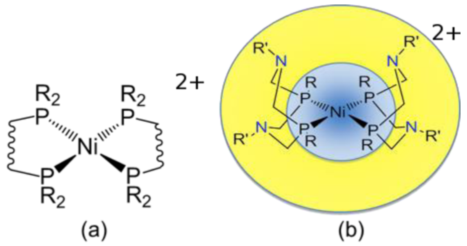

Figure 1. General structure of (a) $[Ni(diphosphine)_2]^{2+}$ complexes (P_2 systems) and (b) $[Ni(P^R{}_2N^{R'}{}_2)_2]^{2+}$ complexes (P_2N_2 systems). In (b), the blue and yellow circles indicate first and second coordination shell ligands, respectively.

members of this class of complexes are not in themselves efficient electrocatalysts for H_2 oxidation/production unless an amine group is included in the outer coordination sphere as an additional catalytic functionality. Therefore, in the present study we extend our earlier investigations to include $[Ni(P^R{}_2N^{R'}{}_2)_2]^{2+}$ electrocatalysts containing 1,5-diaza-3,7-diphosphacyclooctane ligands ($P^R{}_2N^{R'}{}_2$, often referred to as P_2N_2 ligands) with pendant amines positioned in close proximity to the metal center in the second coordination sphere (Figure 1b) where the amines interact with a metal-bound substrate, but do not directly bind to the metal center. It has been shown that pendant amines incorporated into six-membered rings, defined by the metal center and the diphosphine ligands, facilitates heterolytic cleavage or formation of the H−H bond while serving as relays for proton transfers in the catalytic oxidation and production of H_2.[23−25] For these P_2N_2 based complexes, the catalytic activity occurs at much higher rates and/or lower overpotentials compared to P_2 catalysts that have no pendant amines, indicating the critical role of proton relays in lowering barriers for these catalytic reactions.[13,15,16,19] The role of pendant amines in several other classes of metal complexes that are electrocatalysts for production of H_2[26−31] or oxidation of H_2[32−34] has been demonstrated, providing strong evidence that pendant amines functioning as proton relays can profoundly influence reaction pathways and energetics.

The catalytic cycle for H_2 oxidation and production by $[Ni(P^R{}_2N^{R'}{}_2)_2]^{2+}$ complexes, as the result of extensive experimental[8,10−13] and theoretical investigations,[19,23,24,35−40] is reported in Figure 2. Computational studies of the $[Ni(P^R{}_2N^{R'}{}_2)_2]^{2+}$ catalytic activity showed that H_2 oxidation proceeds with the formation of a transient H_2 adduct, which undergoes heterolytic H_2 splitting with the formation of a N-protonated nickel hydride species (proton/hydride species, denoted **e/NiH**$^{2+}$ where **e** indicates an endo conformation of the N−H bond with respect to the metal). The latter easily evolves toward a doubly protonated Ni(0) species, where both protons are oriented endo (denoted **e/e**$^{2+}$). Two proton and electron transfers (or proton-coupled electron transfers)[37,38,41] complete the catalytic cycle. A potential H_2 evolution mechanism follows this same cycle in a counterclockwise fashion, as represented by the central cycle in Figure 2, with the two initial reduction/protonation steps. However, the existence of multiple protonation sites gives rise to species with protons that are not properly positioned and are detrimental to catalysis as shown by the arrows on the left side of Figure 2. As illustrated, protonation can take place either endo (denoted with an **e**) to the metal center or exo (denoted with an **x**) to the metal center, which leads to the production of mono protonated exo isomers (**x**$^+$) and doubly protonated exo/exo isomers (**x/x**$^{2+}$) or endo/exo isomers (**e/x**$^{2+}$) (Figure 2).[35] Only protonated pendant amines having an endo geometry are properly positioned to function efficiently as proton relays during catalysis[36,42] and isomers with exo positioned protons must undergo deprotonation/protonation to form endo protonated intermediates for catalysis to occur.

Our goal is to develop a simple predictive model that allows the calculation of the relative free energy of potential intermediates ("free energy maps") using a minimal number of easily determined parameters. Using such maps, the free energy profile along the catalytic cycle can be easily

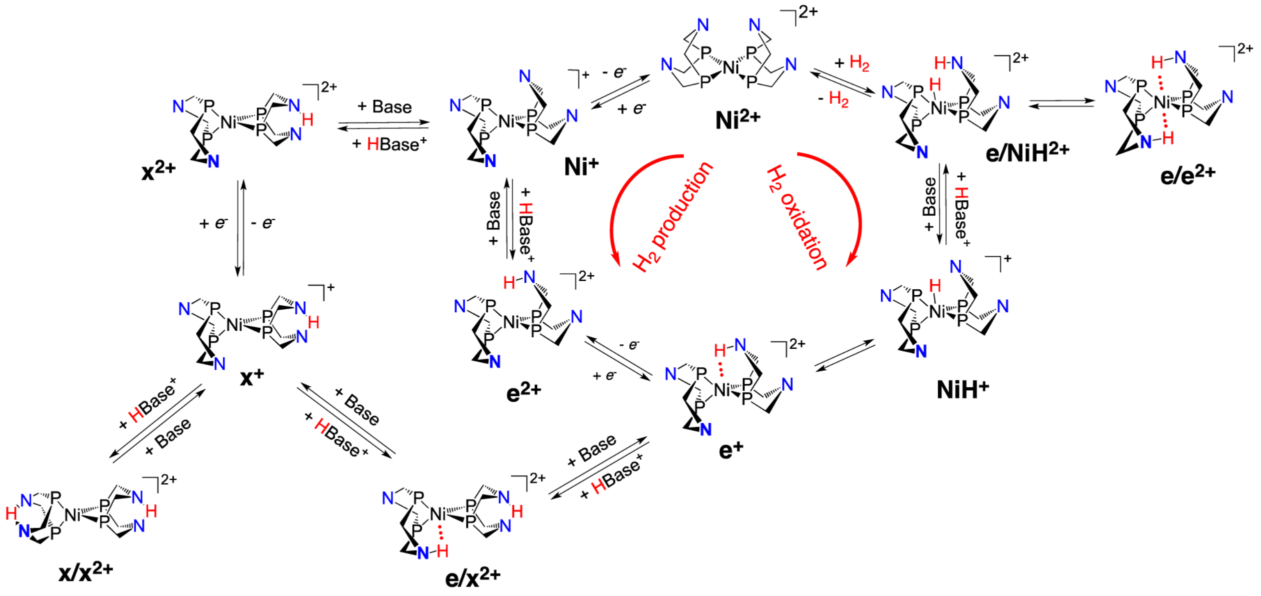

Figure 2. Proposed catalytic cycle for H_2 oxidation (clockwise) and H_2 production (counterclockwise) by $[Ni(P^R{}_2N^{R'}{}_2)_2]^{2+}$ electrocatalysts. In this example H_2 production follows a stepwise electron−proton−electron−proton sequence of steps. Protonation of exo positions results in branching to less productive pathways. N and P substituents are not shown for clarity.

constructed, therefore readily permitting the prediction of low- or high-energy intermediates, and possibly suggesting ways to avoid such undesired species.[7,43,44] Moreover, knowledge of the relative free energy of the intermediates, under standard conditions, can be used to extrapolate these quantities under different experimental conditions (i.e., change of pH, H_2 partial pressure, applied electrical potential) and can thus serve as a guide for optimizing the reaction conditions. The ability to construct a comprehensive free energy map relies on the understanding of thermodynamic properties such as bond strengths and redox potentials. In principle, the thermodynamic properties can be determined through experimental measurements and/or computations. The systematic measurement of the thermodynamic properties needed to build these maps is challenging, being possible only for a few of them (e.g., the Ni(II)/Ni(I) and Ni(I)/Ni(0) reduction potentials), and it is limited to experimentally observable intermediates. In this context, computations can provide access to these properties, but only if one has the confidence that the calculated values are within a useful range of accuracy.

In our previous work,[22] we developed a theoretical protocol based on density functional theory (DFT) calculations and an isodesmic approach for the accurate (within 2 kcal/mol) computational determination of the thermodynamic quantities across a series of P_2 systems. We have also shown that all thermodynamic properties required to predict the relative free energies of intermediates correlate with either Ni(II)/Ni(I) and/or Ni(I)/Ni(0) redox potentials. Using these correlations, and appropriate thermodynamics cycles, the relative free energies of all of the relevant species involved in catalysis can be predicted with a high degree of confidence from the potentials of the Ni(II/I) and Ni(I/0) couples, which are easily measured by experiment. To extend this study to complexes with pendant amines and build a predictive model, it is necessary to study both the energetics of the protonation of the pendant amines, and how this is influenced by the electronics at the metal center, and conversely the influence of the pendant amines on the metal center properties.

In this paper, we examine the thermodynamic properties of the first coordination sphere, and how the incorporated pendant amine affects the thermodynamics properties of the Ni center. We then calculate the pK_a of the protonated pendant amine of P_2N_2 systems and explore the correlations of this quantity with the Ni(II)/Ni(I) and/or Ni(I)/Ni(0) redox potentials to understand the electronic factors influencing it. From this knowledge, we construct a model capable of predicting relative thermodynamics of all the potential catalytic intermediates shown in Figure 3 using three parameters, the potentials of the Ni(II)/Ni(I) and Ni(I)/Ni(0) redox couples and the pK_a values of a parent aminium (R′-NH_3^+) from which the ligand is derived. We then discuss some applications of this predictive model and demonstrate how the information provided by this analysis can reveal the intimate interconnections between catalytic pathways (and side products), which are a requisite for improved catalyst design.

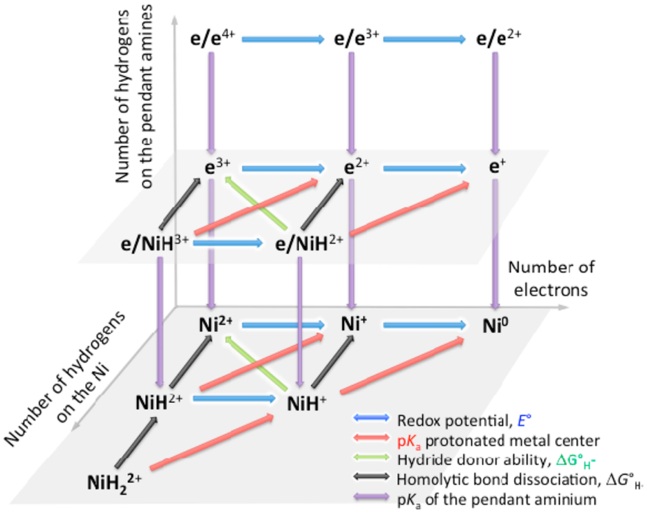

Figure 3. Thermodynamic map connecting all the metal-protonated and endo-protonated $[H_nNi(P^R{}_2N^{R'}{}_2)_2H_m]^{q+}$ species. The abbreviations used for the different species are shown in Figure 2. **NiH_2^{2+}** represents $[H_2Ni^{IV}(P_2N_2)_2]^{2+}$, **$NiH^{2+}$** represents $[HNi^{III}(P_2N_2)_2]^{2+}$, and **$e/NiH^{3+}$** represents *endo*-$[HNi^{III}(P_2N_2)(P_2N_2H)]^{3+}$. Blue arrows: electron transfer reactions with associated potentials; Black arrows: homolytic Ni−H bond dissociations with associated free energies; Green arrows: hydride transfer reactions with associated free energies; Red arrows: deprotonation of Ni-hydrides with associated pK_a values; Violet arrows: deprotonation of pendant aminium(s) with associated pK_a values.

2. COMPUTATIONAL METHODS

2.1. Complexes and Nomenclature.

The systems studied in this paper are Ni complexes with $P^R{}_2N^{R'}{}_2$ ligands. We investigated both known complexes and hypothetical ones not yet synthesized. For the hypothetical complexes, a similar strategy to that employed for the P_2 systems[24] was applied by using the fluorinated methyl groups as substituents on P and N atoms, allowing us to investigate systemically the effects of the nature of substituents and consolidate the correlations with an extended set of data. Figure 3 depicts the thermodynamic diagram connecting the potential intermediates resulting from protonation of the Ni center and endo protonation of the pendant amines, along with the associated thermodynamic properties examined in this study. A more comprehensive diagram including the possibility of exo protonation is provided in **Figure S1** of the Supporting Information. In Figure 3 the potential intermediates are organized as follows: along the x axis is the change in the charge on the metal center as a result of electron transfer; along the y axis is the change in the number of hydrogens bound to Ni; and along the z axis is the change in the number of protons on the N atoms of the ligand. The structures of all of the species studied are given in **Scheme SI-1** of the Supporting Information. Nonprotonated Ni(II), Ni(I), and Ni(0) complexes are simply referred as **Ni^{2+}**, **Ni^+**, **Ni^0**. We use the letters **e** and **x** to indicate isomers protonated on N in the endo and exo positions respectively, whereas **NiH** indicates the presence of a nickel hydride. While referring to the various species identified by the letter code, the overall charge of the complex is also provided. For example, **e/NiH^{2+}** stands for a complex with an endo-protonated N atom, a hydrogen bound to Ni, and a total charge of 2+, whereas **e^{2+}** stands for the singly endo protonated Ni(I) intermediate (see Figure 2 and **Scheme S1** of the Supporting Information). Note that double protonation of the same ligand is generally energetically unfavorable[36] and not considered, though one example of a doubly protonated ligand has been reported at −70 °C.[45]

The following symbols are used for the thermodynamic quantities considered in the present work: Reduction potentials, E^0, hydride donor abilities, $\Delta G°_{H^-}$, homolytic Ni−H bond dissociation energies, $\Delta G°_{H\cdot}$, and pK_a values. To

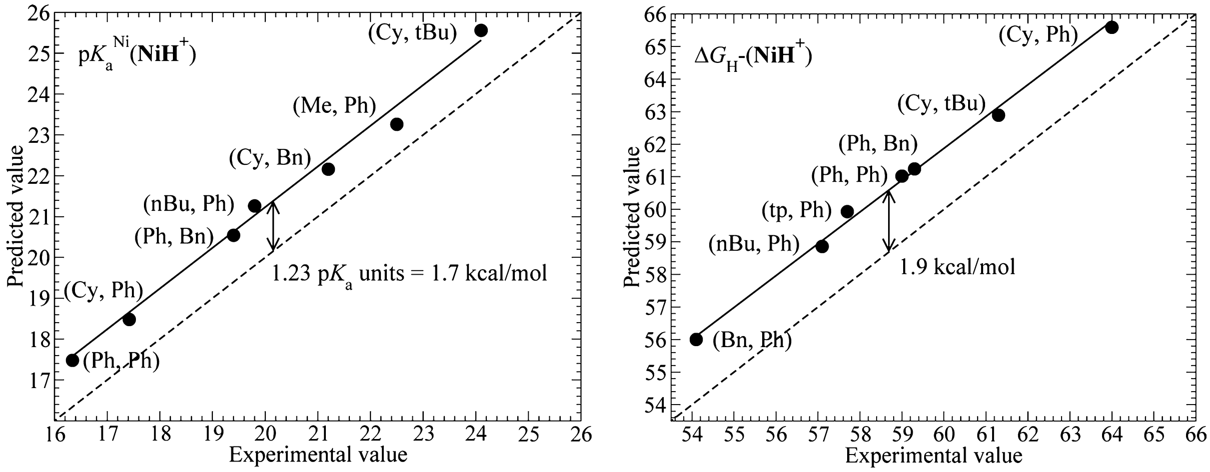

Figure 4. Computed pK_a^{Ni}(**NiH$^+$**) and hydride donor ability, ΔG_{H^-}(**NiH$^+$**) (in kcal/mol), for $[HNi(P^R{}_2N^{R'}{}_2)_2]^+$ complexes using the linear free energy correlations inferred for P_2 systems vs the experimental values (solid circles). The solid line is a least-squares fit to the data, and the dashed line is the 1:1 line that would be expected if the N atoms introduced no perturbation. The labels indicate the (R, R′) substituents on the P and N atoms of each catalyst, where Me = methyl, Cy = cyclohexyl, nBu = *n*-butyl, tBu = *t*-butyl, tp = 2,2,4-trimethylpentyl, Bn = benzyl, and Ph = phenyl.

distinguish the pK_a of Ni–H and that of N–H, the superscript "Ni" is added for the former, whereas the superscripts "e" and "x" are specified when referring to endo and exo protonated pendant amine, respectively. For example, the thermodynamic properties associated with **e/NiH^{2+}**, which has one proton on the Ni center and one on a pendant amine, are defined in eqs 1–5.

$$\mathbf{e/NiH^{2+}} \rightleftharpoons \mathbf{e^+} + H^+ \qquad pK_a^{Ni}(\mathbf{e/NiH^{2+}}) \tag{1}$$

$$\mathbf{e/NiH^{2+}} \rightleftharpoons \mathbf{NiH^+} + H^+ \qquad pK_a^{e}(\mathbf{e/NiH^{2+}}) \tag{2}$$

$$\mathbf{e/NiH^{2+}} \rightleftharpoons \mathbf{e^{2+}} + H\bullet \qquad \Delta G^\circ{}_{H\bullet}(\mathbf{e/NiH^{2+}}) \tag{3}$$

$$\mathbf{e/NiH^{2+}} \rightleftharpoons \mathbf{e^{3+}} + H^- \qquad \Delta G^\circ{}_{H^-}(\mathbf{e/NiH^{2+}}) \tag{4}$$

$$\mathbf{e/NiH^{2+}} + e^- \rightleftharpoons \mathbf{e/NiH^+} \qquad E^\circ{}_{II/I}(\mathbf{e/NiH^{2+}}) \tag{5}$$

Herein all redox potentials are given with respect to the ferrocenium/ferrocene couple in acetonitrile solvent.

2.2. Procedure for Calculating Thermodynamic Properties. In accord with the reported experimental free energies, all calculated reaction free energies are quoted at the standard state (T = 298 K, p = 1 atm of H_2, 1 mol/L concentration of all species in acetonitrile).

Thermodynamic quantities associated with species having hydrogen bound to the Ni center (e.g., the properties in the bottom layer of the diagram in Figure 3) were calculated from the free energies of isodesmic reactions where $[H_nNi(dmpp)_2]^{q+}$ was used as the reference system (dmpp = 1,3-bis(dimethylphosphino)propane). This procedure was described in previous reports,[22,46,47] and is briefly summarized in the Supporting Information (Section SI-1). The pK_a values for the protonated pendant amine complexes are calculated by a similar isodesmic approach where our reference value is chosen to be that of protonated pyridine ($C_5H_5NH^+$, pK_a = 12.5 in acetonitrile).[48]

All other thermodynamic properties can be obtained from thermodynamic cycles. An example of the calculation of pK_a^{Ni}(**e/NiH^{2+}**) is given below in eqs 6a–6d

$$\mathbf{NiH^+} \rightleftharpoons \mathbf{Ni^0} + H^+ \qquad pK_a^{Ni}(\mathbf{NiH^+}) \tag{6a}$$

$$\mathbf{e/NiH^{2+}} \rightleftharpoons \mathbf{NiH^+} + H^+ \qquad pK_a^{e}(\mathbf{e/NiH^{2+}}) \tag{6b}$$

$$\mathbf{Ni^0} + H^+ \rightleftharpoons \mathbf{e^+} \qquad -pK_a^{e}(\mathbf{e^+}) \tag{6c}$$

$$\mathbf{e/NiH^{2+}} \rightleftharpoons \mathbf{e^+} + H^- \qquad pK_a^{Ni}(\mathbf{e/NiH^{2+}}) = pK_a^{Ni}(\mathbf{NiH^+}) + pK_a^{e}(\mathbf{e/NiH^{2+}}) - pK_a^{e}(\mathbf{e^+}) \tag{6d}$$

It is important to clarify that the pK_a values defined in Figure 3 do not necessarily represent the thermodynamic (experimentally measured) pK_a's, which are related only to lowest free energy species (either reactants or products). For instance, deprotonation of doubly protonated **e/e^{2+}** species result in the **NiH$^+$** hydride species so that the experimental pK_a for **e/e^{2+}** is different from the pK_a^e(**e/e^{2+}**) defined in Figure 3. However, the experimental pK_a can be easily obtained from Figure 3 using simple thermodynamic considerations as discussed in the Supporting Information (Section SI-5).

Experimental observations show that in acetonitrile solution, the solvent coordinates to the Ni(II) center.[13,36] Accordingly all of the calculations involving Ni(II) species were done on five-coordinate complexes with an acetonitrile molecule as the fifth ligand. A discussion on how the fifth ligand influences the redox properties of Ni(II) complexes is provided in the Supporting Information (Section SI-2).

2.3. Density Functional Theory Calculations. Molecular structures were optimized at the DFT level of theory with the hybrid B3P86 exchange and correlation functional[49−51] and the Stuttgart–Dresden relativistic effective core potential and associated basis set (SDD)[52] for Ni, and 6-31G* for all nonmetal atoms.[53] We include an additional polarization p function on hydride (or proton if bound to the amine group) H atoms. Harmonic vibrational frequencies were calculated at the optimized geometries using the same level of theory to estimate the zero-point energy and the thermal contributions (298 K and 1 atm) to the gas-phase free energy. Free energies of solvation in acetonitrile were then computed using a self-consistent reaction field model at the same level of theory as for the other steps. The Conductor-like Polarizable Continuum Model (CPCM)[54,55] was used with Bondi radii.[56] Standard state corrections were applied to solvation free energies. This level of theory has been tested extensively in previous studies and proved to work well for this class of compounds.[22−24,46] All the calculations were carried out with Gaussian 09.[57] The effect of the applied potential was considered adding the customary electrochemical free energy term[58] $\Delta G_{el} = -nFE$, where n is the number of electrons transferred (H_2 production), F is the Faraday constant, and E is the applied potential with respect to the ferrocenium/ferrocene couple.

3. RESULTS

In this section we focus our discussion on computational results, deferring more detailed connections to experimental observations and applications to catalysis to Section 4. Unless otherwise stated all correlation presented here are derived entirely from computed quantities.

3.1. Thermodynamic Properties for the First Coordination Sphere. The common coordination feature between the P_2 system and the first coordination sphere of the P_2N_2 system stimulates us to ask whether the set of correlations previously developed for P_2 systems be applied to predict the corresponding quantities of P_2N_2 systems. Figure 4 shows plots of experimental pK_a^{Ni}(**NiH$^+$**) and $\Delta G°_{H^-}$(**NiH$^+$**) values of P_2N_2 systems versus those computed from the formulas based on P_2 systems[24] (solid circles and line). These data differ from the dotted line, which represents the correlation expected for the P_2 systems, that is, if the N atoms introduced no perturbation. As can be seen, there is a clear and systematic variance of approximately 2 kcal/mol.

This discrepancy can be understood by noting that these two properties share the same starting point, that is, the Ni hydride species, **NiH$^+$** (see Figure 5a). Hence, the similar shift in energy for these two properties indicates that the hydride species **NiH$^+$** of P_2N_2 systems are systematically different from those of P_2 systems. This approximately 2 kcal/mol destabilization is traced back to a weak repulsive interaction between the pendant amine and the hydride, which leads the hydride to occupy an equatorial position of a trigonal bipyramid as opposed to an axial one in the P_2 systems (see Figure 5).

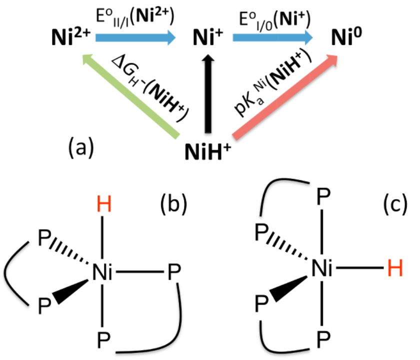

Figure 5. Thermodynamic relationship between nonprotonated nickel complexes and **Ni^{2+}**, **Ni$^+$**, **Ni^0** and the Ni(II) hydride intermediate, **NiH$^+$** (a). Also reported is the coordination geometry of the metal center in the Ni(II) hydride intermediate for P_2 (b) and P_2N_2 complexes (c).

The systematic changes in pK_a^{Ni}(**NiH$^+$**) and ΔG_{H^-}(**NiH$^+$**) resulting from the replacement of P_2 ligands with P_2N_2 ligands suggests that other thermodynamic properties for the first coordination sphere of P_2N_2 systems can also be predicted from the thermodynamic correlations obtained for P_2 systems, with appropriate adjustment of the corresponding intercept of the linear equations from ref 22. We have thus calculated *all* of the thermodynamic properties associated with the first coordination sphere by constructing linear correlations of any property with $E°_{I/0}$(**Ni$^+$**) and $E°_{II/I}$(**Ni^{2+}**), as done previously for the P_2 systems. In Table 1 we present the overall correlations obtained by this process. Note that in the data fitting, we have not constrained the slope to be identical to that of the P_2 systems. That said, the differences in slopes between P_2N_2 and P_2 systems are relatively small (at most 0.06 V) with the major change resulting in the intercepts.

Table 1. Computed Correlations between the Thermodynamic Properties for the First Coordination Sphere of $[Ni(P^R{}_2N^{R'}{}_2)_2]^{2+}$ Complexes^a

property	correlation for P_2N_2 systems
pK_a^{Ni}(**NiH$^+$**)	$-18.00\ E°_{I/0}$(**Ni$^+$**) − 2.00
pK_a^{Ni}(**NiH^{2+}**)	$-18.38\ E°_{I/0}$(**Ni$^+$**) −28.38
pK_a^{Ni}(**NiH$_2^{2+}$**)	$-16.90\ E°_{I/0}$(**Ni$^+$**) −23.38
$\Delta G°_{H^-}$(**NiH$^+$**)	$21.70\ E°_{II/I}$(**Ni^{2+}**) + 77.50
$\Delta G°_{H\cdot}$(**NiH$^+$**)	$-1.51\ E°_{I/0}$(**Ni$^+$**) + 50.59
$\Delta G°_{H\cdot}$(**NiH^{2+}**)	$-25.07\ E°_{I/0}$(**Ni$^+$**) + $23.06\ E°_{II/I}$(**Ni^{2+}**) + 14.15
$\Delta G°_{H\cdot}$(**NiH$_2^{2+}$**)	$0.46\ E°_{I/0}$(**Ni$^+$**) + 58.10
$E°_{III/II}$(**NiH^{2+}**)	$1.02\ E°_{I/0}$(**Ni$^+$**) + 1.51

^{a}Redox potentials in V; Hydride donor ability and homolytic Ni−H bond dissociations in kcal/mol. Note that these equations differ from those for the P_2 systems[22] by only small changes in the slope with more significant changes in intercepts due to the geometric perturbation imposed by the pendent amine (see text for discussion). All correlations are derived from computed quantities.

3.2. First Protonation at a Pendant Amine. With the equations listed in Table 1, we are able to predict the thermodynamic properties associated with the first coordination sphere based on the knowledge of only two redox potentials. However for P_2N_2 systems, protons can interact with both Ni and N atoms, and it is necessary to understand the relative energetics of protonation at both sites for developing efficient catalysts. In this section we discuss the calculations of the pK_a for the protonated pendant amine of P_2N_2 complexes. We first consider the single protonation at the N atoms for the species described in the bottom layer of the thermodynamic diagram shown in Figure 3, resulting in the corresponding species shown in the middle layer. Protonation of dihydride species is not considered because it is unlikely that they are formed under catalytic conditions.[23,24]

We first consider the pK_a of the endo form of the N-protonated Ni(0) species. The P_2N_2 ligands are synthesized from primary amines, and the pK_a values of their conjugate acids (primary aminiums) are readily available from the literature or easy to obtain through experiment or calculation. Here we show that a relationship between the pK_a of the protonated pendant amine and their parent aminium (R′-NH_3^+) exists, and a mathematical expression for this relation is derived. As shown in Figure 6, when the substituents on the P atoms are either CH_3 or CF_3, the pK_a values of the P_2N_2 complexes are linearly correlated with those of their parent aminium. The effect of the R′ groups on the pK_a values is consistent with the electron donor/withdrawing abilities of R′ groups (where R′ = CH_3, CH_2F, CHF_2, CF_3). It is also not surprising that the substituents, R, on P atoms influence the pK_a of pendant amine, and changing R from CH_3 to CF_3 decreases the pK_a values by approximately the same amount regardless of the substituents on N. In addition, the substituent on P can have a strong influence on the electron density at the Ni center as reflected in the Ni (I/0) couple. These considerations

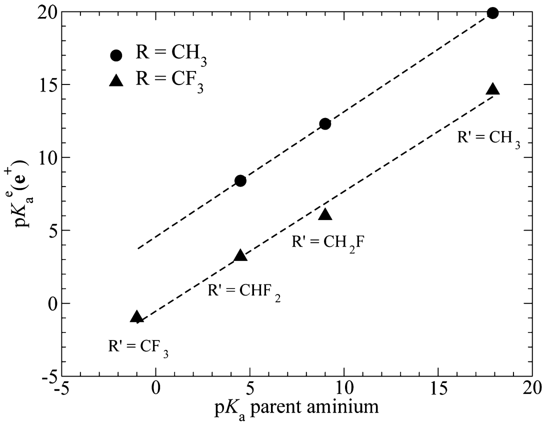

Figure 6. Calculated pK_a of the endo protonated Ni(0) species, **e**$^+$, vs the computed value of the pK_a of the parent aminium $R'NH_3^+$. The R groups are the substituents on P atoms, whereas R′ = CH_3, CH_2F, CHF_2, CF_3 are the substituents on N atoms. Dashed lines are linear least-squares fits to the data.

suggest the possibility of predicting the pK_a values for the protonated pendant amine of the complexes from $E°_{I/0}(\mathbf{Ni}^+)$ and the pK_a values of the parent aminium. Note this is an inference of correlation and not causation as the R groups on the phosphine influence both quantities. To confirm this hypothesis, we calculated pK_a values of a series of P_2N_2 complexes and fit them to these two parameters and obtained eq 7, which gives a standard deviation of 0.5 pK_a units.

$$pK_a^N(\mathbf{e}^+) = 0.69pK_a(R'NH_3^+) - 7.09E°_{I/0}(\mathbf{Ni}^+) - 1.9 \tag{7}$$

Following the same reasoning, we found that the pK_a values for the other singly protonated species have similar properties and can be predicted from the same two parameters, namely, pK_a values of the protonated parent amine and $E°_{I/0}(\mathbf{Ni}^+)$. These equations are listed in Table 2.

Table 2. Computed Correlations between the pK_a Values for Singly Protonated Pendant Amines and the Values of the pK_a of the Parent Aminium, pK_a($R'NH_3^+$), and the Ni(I)/Ni(0) Redox Potential, $E°_{I/0}(\mathbf{Ni}^+)$, for $[Ni(P^R{}_2N^{R'}{}_2)_2]^{2+}$ Complexes

endo	exo
$pK_a^e(\mathbf{e}^+) = 0.69pK_a\ (R'NH_3^+) - 7.09E°_{I/0}(\mathbf{Ni}^+) - 1.9$	$pK_a^x(\mathbf{x}^+) = 0.88pK_a\ (R'NH_3^+) - 6.49E°_{I/0}(\mathbf{Ni}^+) - 4.7$
$pK_a^e(\mathbf{e}^{2+}) = 0.80pK_a\ (R'NH_3^+) - 5.59E°_{I/0}(\mathbf{Ni}^+) - 9.5$	$pK_a^x(\mathbf{x}^{2+}) = 0.91pK_a\ (R'NH_3^+) - 6.58E°_{I/0}(\mathbf{Ni}^+) - 10.3$
$pK_a^e(\mathbf{e}^{3+}) = 0.90pK_a\ (R'NH_3^+) - 8.47E°_{I/0}(\mathbf{Ni}^+) - 17.0$	$pK_a^x(\mathbf{x}^{3+}) = 0.95pK_a\ (R'NH_3^+) - 9.10E°_{I/0}(\mathbf{Ni}^+) - 15.9$
$pK_a^e(\mathbf{e/NiH}^{2+}) = 0.80pK_a\ (R'NH_3^+) - 7.26E°_{I/0}(\mathbf{Ni}^+) - 9.4$	$pK_a^x(\mathbf{x/NiH}^{2+}) = 0.95pK_a\ (R'NH_3^+) - 6.34E°_{I/0}(\mathbf{Ni}^+) - 10.2$
$pK_a^e(\mathbf{e/NiH}^{3+}) = 0.81pK_a\ (R'NH_3^+) - 6.91E°_{I/0}(\mathbf{Ni}^+) - 15.8$	$pK_a^x(\mathbf{x/NiH}^{3+})= 0.86pK_a\ (R'NH_3^+) - 6.81E°_{I/0}(\mathbf{Ni}^+) - 14.8$

The pK_a values for exo protonation show similar correlations with the pK_a values of the parent aminium and $E^0{}_{I/0}(\mathbf{Ni}^+)$ redox potential (Table 2). Compared to the endo-protonated isomers, the dependence on the pK_a values of the parent aminium is larger for exo-protonated isomers, as indicated by the larger coefficients for the pK_a term. This trend reflects a greater dependence on the amine basicity for the proton being chelated by two N atoms of the same ligand. Further comments on the correlation between the acidity of the parent aminium and that of N-protonated catalysts are given in the Supporting Information (Section SI-3).

3.3. Second Protonation at a Pendant Amine. We now consider the second protonation at the pendant amines. Among many possible conformers, only three are studied herein because they are low energy conformers with small energy difference (within 2 kcal/mol) based on our previous theoretical and experimental results.[24,35] The pK_a values are defined according to eq 8 for **e**/**e**$^{2+}$ and similar equations for the other **e**/**x**$^{2+}$ and **x**/**x**$^{2+}$ isomers (Figure 2). Using the same procedures as described above for the monoprotonated species, we found that the pK_a values of the doubly protonated complexes are correlated with the pK_a values of the parent aminium and the $E°_{I/0}(\mathbf{Ni}^+)$ redox potentials, as shown by the equations listed in Table 3.

$$\mathbf{e/e}^{2+} \rightleftharpoons \mathbf{e}^+ + H^+ \quad pK_a^N(\mathbf{e/e}^{2+}) \tag{8}$$

Table 3. Computed Correlations between the pK_a Values for Doubly Protonated Pendant Amines and the Values of the pK_a of the Parent Aminium, pK_a($R'NH_3^+$), and the Ni(I)/Ni(0) Redox Potential, $E°_{I/0}(\mathbf{Ni}^+)$, for $[Ni(P^R{}_2N^{R'}{}_2)_2]^{2+}$ Complexes

Endo–Endo	Exo-Exo
$pK_a^e(\mathbf{e/e}^{2+}) = 0.81pK_a(R'NH_3^+) - 6.02E°_{I/0}(\mathbf{Ni}^+) - 5.0$	$pK_a^x(\mathbf{x/x}^{2+}) = 0.90pK_a(R'NH_3^+) - 6.74E°_{I/0}(\mathbf{Ni}^+)- 6.4$
$pK_a^e(\mathbf{e/e}^{3+}) = 0.84pK_a(R'NH_3^+) - 5.92E°_{I/0}(\mathbf{Ni}^+) - 11.5$	$pK_a^x(\mathbf{x/x}^{3+}) = 0.88pK_a(R'NH_3^+) - 7.43E°_{I/0}(\mathbf{Ni}^+) - 11.8$
$pK_a^e(\mathbf{e/e}^{4+}) = 0.87pK_a(R'NH_3^+) + 1.32E°_{I/0}(\mathbf{Ni}^+) - 13.7$	$pK_a^x(\mathbf{x/x}^{4+}) = 0.94pK_a(R'NH_3^+) - 3.37E°_{I/0}(\mathbf{Ni}^+) - 14.1$
Endo Site of Endo-Exo	Exo Site of Endo-Exo
$pK_a^e(\mathbf{e/x}^{2+}) = 0.75pK_a(R'NH_3^+) - 6.4E°_{I/0}(\mathbf{Ni}^+) - 3.6$	$pK_a^x(\mathbf{e/x}^{2+}) = 0.96pK_a(R'NH_3^+) - 5.1E°_{I/0}(\mathbf{Ni}^+) - 6.2$
$pK_a^e(\mathbf{e/x}^{3+}) = 0.84pK_a(R'NH_3^+) - 5.1E°_{I/0}(\mathbf{Ni}^+) - 10.6$	$pK_a^x(\mathbf{e/x}^{3+}) = 0.94pK_a(R'NH_3^+) - 6.5E°_{I/0}(\mathbf{Ni}^+) - 11.7$
$pK_a^e(\mathbf{e/x}^{4+}) = 0.82pK_a(R'NH_3^+) - 1.4E°_{I/0}(\mathbf{Ni}^+) - 14.2$	$pK_a^x(\mathbf{e/x}^{4+}) = 0.90pK_a(R'NH_3^+) - 2.8E°_{I/0}(\mathbf{Ni}^+) - 13.7$

The pK_a defined in eq 8 is different from that measured experimentally because the singly protonated species **e**$^+$ resulting from the deprotonation of the doubly protonated species (**e**/**e**$^{2+}$ and **e**/**x**$^{2+}$) undergoes an intramolecular proton transfer reaction to form **NiH**$^+$. However the experimentally observed pK_a values can be calculated from a thermodynamic cycle (eqs 9a–9d) using the pK_a value defined in eq 8 and $pK_a^e(\mathbf{e}^+)$ and $pK_a^{Ni}(\mathbf{NiH}^+)$ determined from the equations listed in Tables 1 and 2, respectively. This thermodynamic cycle can be readily constructed from an inspection of the thermodynamic diagram shown in Figure 3.

$$\mathbf{e/e}^{2+} \rightleftharpoons \mathbf{e}^+ + H^+ \qquad pK_a^N(\mathbf{e/e}^{2+}) \tag{9a}$$

$$\mathbf{e}^+ \rightleftharpoons \mathbf{Ni}^0 + H^+ \qquad pK_a^e(\mathbf{e}^+) \tag{9b}$$

$$\mathbf{Ni}^0 + H^+ \rightleftharpoons \mathbf{NiH}^+ \qquad -pK_a^{Ni}(\mathbf{NiH}^+) \tag{9c}$$

$$\mathbf{e/e}^{2+} \rightleftharpoons \mathbf{NiH}^+ + H^+ \qquad pK_a = pK_a^N(\mathbf{e/e}^{2+}) + pK_a^e(\mathbf{e}^+) - pK_a^{Ni}(\mathbf{NiH}^+) \tag{9d}$$

3.4. Effect of Protonation on the Thermodynamic Properties of the First Coordination Sphere. With knowledge of the thermodynamic properties of the first coordination sphere and the pK_a values of protonated pendant amines, we can now examine how the thermodynamic properties for the first coordination sphere are influenced by the protonation at a pendant amine. Using thermodynamic cycles, we derived the equations for predicting the thermodynamic properties described within the middle and top layers of Figure 3 and Supporting Information, Figure S1 (Table 4). All the thermodynamic properties listed in Table 4 can be predicted from the pK_a values of the protonated parent aminium, and two redox potentials, $E^\circ_{I/0}(\mathbf{Ni}^+)$ and $E^\circ_{II/I}(\mathbf{Ni}^{2+})$. It can be seen from the intercepts of the equations in Table 4 that protonation results in positive shifts of the potentials for both the Ni(II/I) and the Ni(I/0) couples with larger shifts for the doubly protonated species[21,59] [e.g. $E^\circ_{I/0}(\mathbf{e}/\mathbf{e}^{3+})$] compared to the mono protonated species [*e.g.* $E^\circ_{I/0}(\mathbf{e}^{2+})$]. In addition, the constants for both the mono and the doubly protonated species indicate that endo protonation results in more positive shifts than exo protonation. Significant experimental data is only available for the $E^\circ_{I/0}$ couples of the doubly protonated species ($E^\circ_{I/0}(\mathbf{e}/\mathbf{e}^{3+})$, $E^\circ_{I/0}(\mathbf{e}/\mathbf{x}^{3+})$, and $E^\circ_{I/0}(\mathbf{x}/\mathbf{x}^{3+})$). In this case, the difference in the redox potentials for the three different isomers has been interpreted in terms of hydrogen bonding between the protonated pendant amine and the Ni(0) center. The $\mathbf{e}/\mathbf{e}^{2+}$ isomer has two hydrogen bonds to Ni(0), the $\mathbf{e}/\mathbf{x}^{2+}$ isomer has one hydrogen bond to Ni(0), and the $\mathbf{x}/\mathbf{x}^{2+}$ isomer has no hydrogen bonds to Ni(0). These hydrogen bonds between Ni(0) and protons on the pendant amines remove electron density from the Ni center and result in more positive redox potentials. As expected the hydride donor abilities of the protonated hydride complexes are decreased ($\Delta G^\circ_{H^-}$ is larger) with respect to the corresponding unprotonated species, and the pK_a values for the deprotonation of the Ni center are decreased when the amines are protonated.

Table 4. Correlations Derived from the Thermodynamic Cycles Using Equations in Tables 1−3[a]

Endo/Endo-Endo

$E^\circ_{I/0}(\mathbf{e}^{2+}) = -0.006\text{p}K_a(\text{R}'\text{NH}_3^+) + 0.91E^\circ_{I/0}(\mathbf{Ni}^+) + 0.45$

$E^\circ_{II/I}(\mathbf{e}^{3+}) = -0.006\text{p}K_a(\text{R}'\text{NH}_3^+) + 0.17E^\circ_{I/0}(\mathbf{Ni}^+) + E^\circ_{II/I}(\mathbf{Ni}^{2+}) + 0.45$

$\text{p}K_a^{\text{Ni}}(\mathbf{e}/\mathbf{NiH}^{2+}) = 0.110\text{p}K_a(\text{R}'\text{NH}_3^+) - 18.17E^\circ_{I/0}(\mathbf{Ni}^+) - 9.54$

$\Delta G^0_{H^-}(\mathbf{e}/\mathbf{NiH}^{2+}) = -0.135\text{p}K_a(\text{R}'\text{NH}_3^+) + 1.65E^\circ_{I/0}(\mathbf{Ni}^+) + 21.72E^\circ_{II/I}(\mathbf{Ni}^{2+}) + 87.84$

$\Delta G^0_{H\cdot}(\mathbf{e}/\mathbf{NiH}^{2+}) = 0.005\text{p}K_a(\text{R}'\text{NH}_3^+) - 3.79E^\circ_{I/0}(\mathbf{Ni}^+) + 50.7$

$E^\circ_{III/II}(\mathbf{e}/\mathbf{NiH}^{3+}) = E^\circ_{I/0}(\mathbf{Ni}^+) + 1.89$

$\text{p}K_a^{\text{Ni}}(\mathbf{e}/\mathbf{NiH}^{2+}) = 0.012\text{p}K_a(\text{R}'\text{NH}_3^+) - 19.71E^\circ_{I/0}(\mathbf{Ni}^+) - 35.1$

$\Delta G^0_{H\cdot}(\mathbf{e}/\mathbf{NiH}^{3+}) = -0.124\text{p}K_a(\text{R}'\text{NH}_3^+) - 22.95E^\circ_{I/0}(\mathbf{Ni}^+) + 23.06E^\circ_{II/I}(\mathbf{Ni}^{2+}) + 15.8$

$E^\circ_{I/0}(\mathbf{e}/\mathbf{e}^{3+}) = -0.008\text{p}K_a(\text{R}'\text{NH}_3^+) + 0.91\ E^\circ_{I/0}(\mathbf{Ni}^+) + 0.83$

$E^\circ_{II/I}(\mathbf{e}/\mathbf{e}^{4+}) = -0.008\text{p}K_a(\text{R}'\text{NH}_3^+) - 0.26E^\circ_{I/0}(\mathbf{Ni}^+) + E^\circ_{II/I}(\mathbf{Ni}^{2+}) + 0.57$

Exo/Exo-Exo

$E^\circ_{I/0}(\mathbf{x}^{2+}) = -0.001\text{p}K_a(\text{R}'\text{NH}_3^+) + E^\circ_{I/0}(\mathbf{Ni}^+) + 0.33$

$E^\circ_{II/I}(\mathbf{x}^{3+}) = -0.003\text{p}K_a(\text{R}'\text{NH}_3^+) + 0.15E^\circ_{I/0}(\mathbf{Ni}^+) + E^\circ_{II/I}(\mathbf{Ni}^{2+}) + 0.33$

$\text{p}K_a^{\text{Ni}}(\mathbf{x}/\mathbf{NiH}^{2+}) = 0.064\text{p}K_a(\text{R}'\text{NH}_3^+) - 17.85E^\circ_{I/0}(\mathbf{Ni}^+) - 7.5$

$\Delta G^0_{H^-}(\mathbf{x}/\mathbf{NiH}^{2+}) = -0.004\text{p}K_a(\text{R}'\text{NH}_3^+) + 3.76E^\circ_{I/0}(\mathbf{Ni}^+) + 21.72E^\circ_{II/I}(\mathbf{Ni}^{2+}) + 85.3$

$\Delta G^0_{H\cdot}\ (\mathbf{x}/\mathbf{NiH}^{2+}) = 0.055\text{p}K_a(\text{R}'\text{NH}_3^+) - 1.19E^\circ_{I/0}(\mathbf{Ni}^+) + 50.6$

$E^\circ_{III/II}(\mathbf{x}/\mathbf{NiH}^{3+}) = 0.005\text{p}K_a(\text{R}'\text{NH}_3^+) + 1.05E^\circ_{I/0}(\mathbf{Ni}^+) + 1.78$

$\text{p}K_a^{\text{Ni}}(\mathbf{x}/\mathbf{NiH}^{3+}) = -0.051\text{p}K_a(\text{R}'\text{NH}_3^+) -18.61E^\circ_{I/0}(\mathbf{Ni}^+) - 33.4$

$\Delta G^0_{H\cdot}(\mathbf{x}/\mathbf{NiH}^{3+}) = -0.128\text{p}K_a(\text{R}'\text{NH}_3^+) - 21.94E^\circ_{I/0}(\mathbf{Ni}^+) + 23.06E^\circ_{II/I}(\mathbf{Ni}^{2+}) + 15.6$

$E^\circ_{I/0}(\mathbf{x}/\mathbf{x}^{3+}) = -0.001\text{p}K_a(\text{R}'\text{NH}_3^+) + 1.05\ E^\circ_{I/0}(\mathbf{Ni}^+) + 0.65$

$E^\circ_{II/I}(\mathbf{x}/\mathbf{x}^{4+}) = -0.006\text{p}K_a(\text{R}'\text{NH}_3^+) - 0.09E^\circ_{I/0}(\mathbf{Ni}^+) + E^\circ_{II/I}(\mathbf{Ni}^{2+}) + 0.47$

Endo-Exo

$E^\circ_{I/0}(\mathbf{e}/\mathbf{x}^{3+}) = -0.007\text{p}K_a(\text{R}'\text{NH}_3^+) + 0.93E^\circ_{I/0}(\mathbf{Ni}^+) + 0.74$

$E^\circ_{II/I}(\mathbf{e}/\mathbf{x}^{4+}) = -0.001\text{p}K_a(\text{R}'\text{NH}_3^+) - 0.07E^\circ_{I/0}(\mathbf{Ni}^+) + E^\circ_{II/I}(\mathbf{Ni}^{2+}) + 0.55$

[a] Redox potentials E^0 in V relative to the ferrocenium/ferrocene redox couple; Hydricities $\Delta G^0_{H^-}$ and homolytic bond dissociations $\Delta G^0_{H\cdot}$ in kcal/mol; pK_a values in pK_a units.

Overall a comparison of the equations listed in Table 2 indicates that protonation of a reduced Ni species is more favorable than protonation of the Ni(II) complex, that is, the overall charge on the complex is the most important feature determining the pK_a values of the protonated pendant amines. This feature is reflected in the constants of the equations listed in Table 2 (−2 to −5 for $\mathbf{e}^+$ and $\mathbf{x}^+$; −9 to −10 for $\mathbf{e}^{2+}$, $\mathbf{x}^{2+}$, $\mathbf{e}/\mathbf{NiH}^{2+}$, and $\mathbf{x}/\mathbf{NiH}^{2+}$; and −15 to −17 for $\mathbf{e}^{3+}$, $\mathbf{x}^{3+}$, $\mathbf{e}/\mathbf{NiH}^{3+}$, and $\mathbf{x}/\mathbf{NiH}^{3+}$). This is a general observation, which holds for any protonation state (i.e., single and double protonation) and protonation site (e.g., endo vs exo protonation).

4. APPLICATIONS OF THE CORRELATIONS

We presented above the calculations of the thermodynamic properties of $[\text{Ni}(\text{P}^{\text{R}}_2\text{N}^{\text{R}'}_2)_2]^{2+}$ complexes and the correlations among them. All the thermodynamic properties described in the diagram shown in Figure 3 and Supporting Information, Figure S1 can be predicted with only three, readily available (both experimentally and theoretically) quantities, namely, the two redox potentials $E^\circ_{II/I}(\mathbf{Ni}^{2+})$ and $E^\circ_{I/0}(\mathbf{Ni}^+)$, and the p$K_a$ of the parent aminium, pK_a(R′NH$_3^+$). It is remarkable that the majority of the properties can be predicted only from the knowledge of $E^\circ_{I/0}(\mathbf{Ni}^+)$ and pK_a(R′NH$_3^+$). Using the proposed correlations any thermodynamic quantity relevant to mechanistic predictions can be readily and accurately determined.[43,44] For instance, the free energy of formation of protonated intermediates upon H_2 addition to $\mathbf{Ni}^{2+}$ can be predicted with an error smaller than 1 kcal/mol. Similarly, pK_a values can be calculated with an error smaller than 1 pK_a unit. Detailed comparison of measured and calculated thermodynamic quantities are provided in sections SI-4 and SI-5 of the Supporting Information. Instead, we will focus the current discussion on applying the thermodynamic model to obtain mechanistic insights needed for catalyst design.

4.1. Free Energy Maps and Reaction Pathways. The following examples will focus on using these thermodynamic data to obtain mechanistic insights. The redox process for the catalytic H_2 production and oxidation is shown in eq 10.

$$2\text{BH} + 2e^- \rightleftharpoons 2\text{B} + \text{H}_2 \tag{10}$$

For a given protic acid (BH$^+$) under 1.0 atm H_2, the thermodynamic potential of this reaction depends only on the acid used. However for the $[\text{Ni}(\text{P}^{\text{R}}_2\text{N}^{\text{R}'}_2)_2]^{2+}$ catalysts there are many different possible catalytic pathways. One of our goals is to identify the most favorable pathway and understand the factors controlling the rate-limiting step(s) and electrochemical overpotential.[60] Here we refer to overpotential, in the same way as typically employed in molecular electrocatalysis, as the difference between the potential at which catalysis is observed, E, and the equilibrium thermodynamic potential, $E^\circ(\text{BH}^+/\text{B};\text{H}_2)$. A more detailed discussion of this point has been elaborated in our recent studies comparing results from cyclic voltammetry and open circuit potential measurements.[61] The thermodynamic potential can be related to the pK_a of the acid BH$^+$ via eq 11:

$$E^\circ(\text{BH}^+/\text{B};\ \text{H}_2) = E^\circ(\text{H}^+/\text{H}_2) - 2.3(RT/F)\text{p}K_a(\text{BH}^+) \tag{11}$$

where $E^\circ(\text{H}^+/\text{H}_2)$ is the potential of the standard hydrogen electrode in acetonitrile (−0.028 V vs ferrocenium/ferrocene couple),[61] F is the Faraday constant, R is the ideal gas constant,

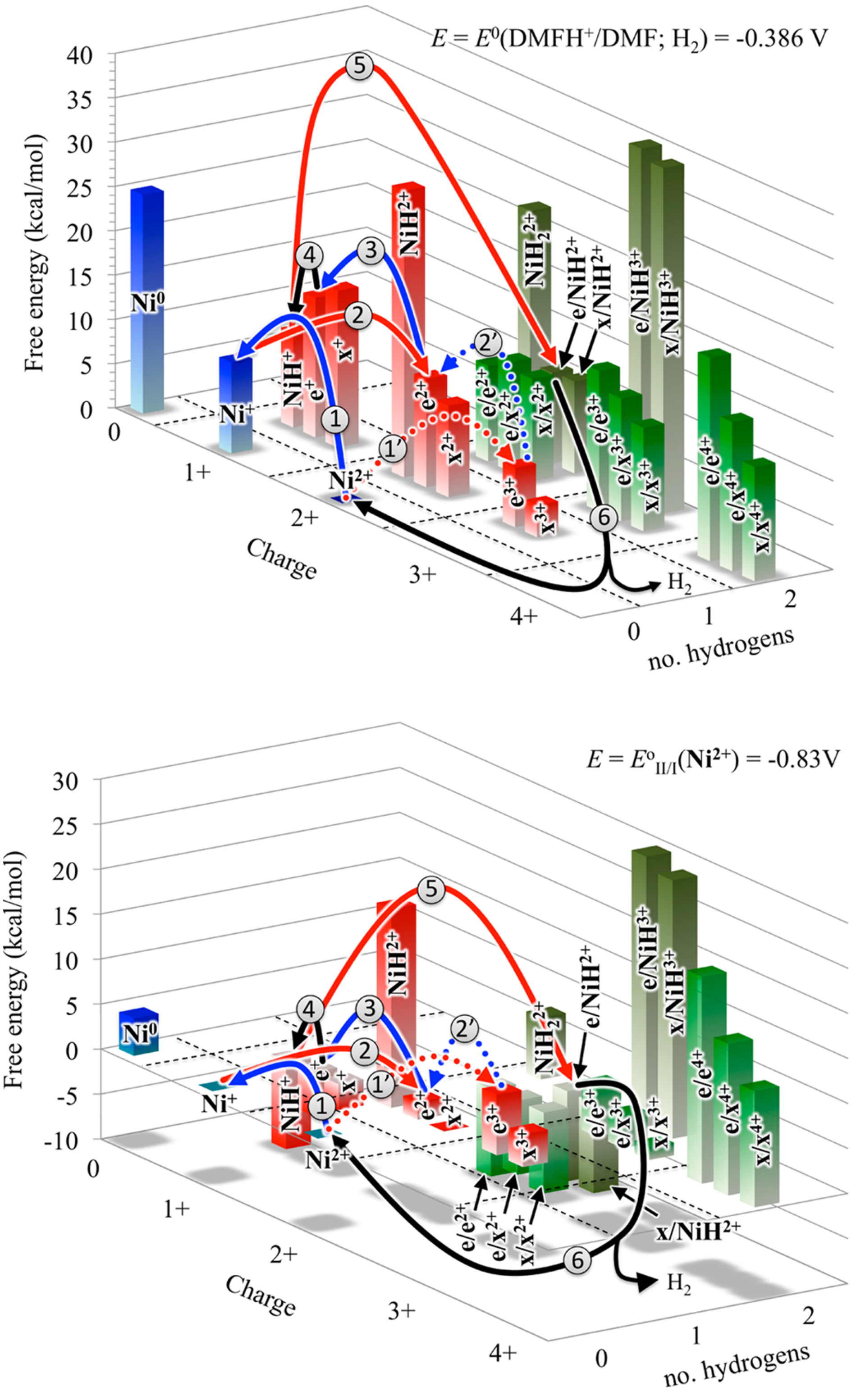

Figure 7. Free energy diagram showing the relative energy of all the possible species originated during catalysis. Data refers to $[Ni(P^{Ph}{}_2N^{Ph}{}_2)_2]^{2+}$ with $DMFH^+$ as external acid at standard conditions under 1 atm H_2. Upper panel: Free energies at the thermodynamic potential for the $2DMFH^+ + 2\ e^- \rightleftharpoons 2\ DMF + H_2$ reaction, $E = E°(DMFH^+/DMF;H_2) = -0.386$ V (i.e., at zero overpotential); Lower panel: Free energies at $E = E°_{II/I}(\mathbf{Ni^{2+}}) = -0.83$ V. The EPEP reaction pathway for endo protonation only is highlighted with solid arrows (steps 1 to 6). Nonprotonated, singly protonated and doubly protonated species are indicated as blue, red, and green bars, respectively. The direction of the color gradient follows the sign of the free energy change (white corresponds to zero relative free energy). The first two steps for the PEEP pathway (steps 1′ and 2′) are highlighted with dotted lines. The color code for the arrows is as follows: Blue lines indicate electron (E) transfer steps; Red lines indicate protonation (P) steps; Black lines indicate intramolecular proton movements and H_2 formation.

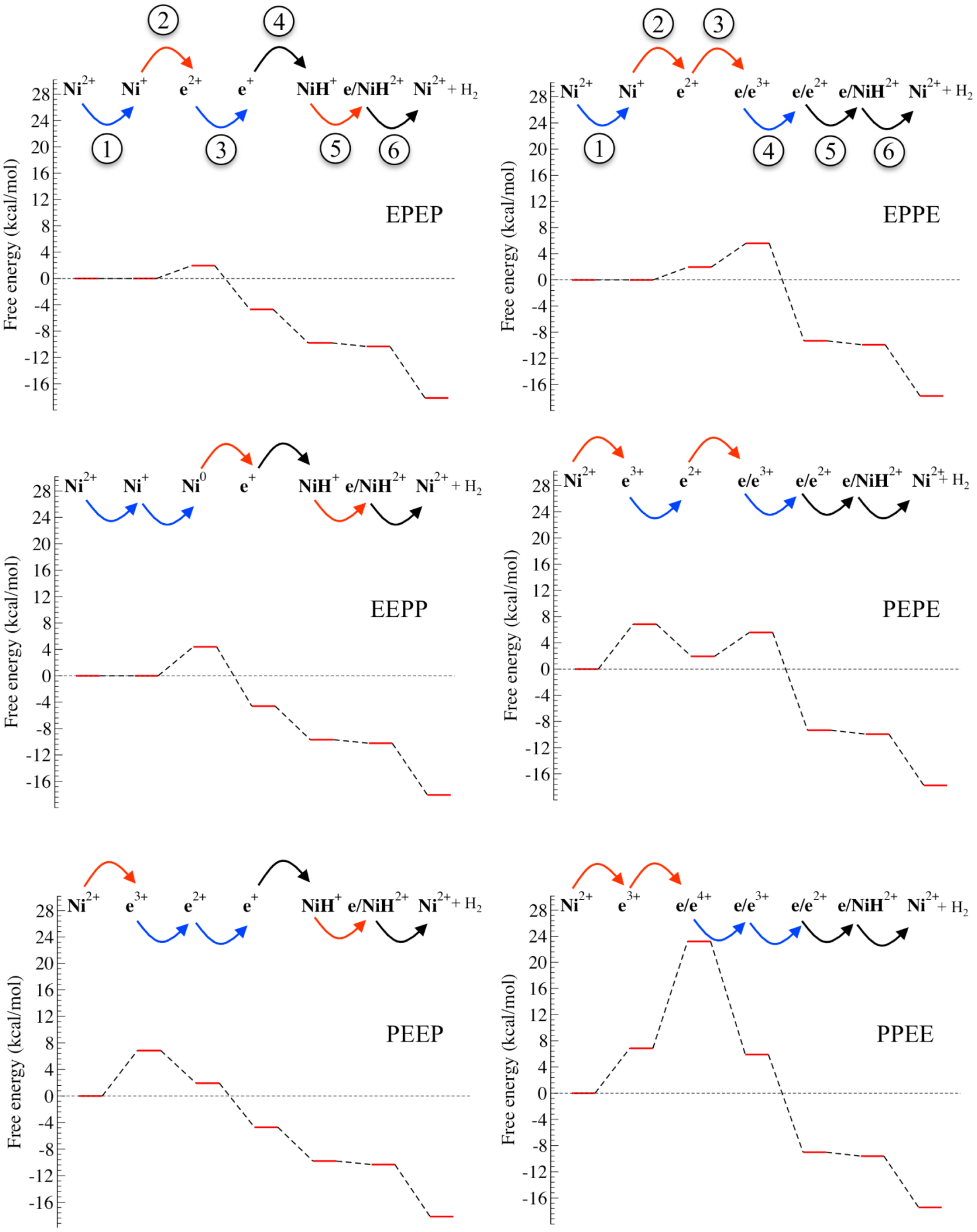

Figure 8. Reaction pathways for H_2 production from $DMFH^+$ ($pK_a = 6.1$) catalyzed by $[Ni(P^{Ph}{}_2N^{Ph}{}_2)_2]^{2+}$ at the applied potential $E = E°_{II/I}(\mathbf{Ni^{2+}}) = -0.83$ V. Only endo protonation is considered. Blue arrow: electron transfer; red arrows: protonation step; black arrow: intramolecular proton movement.

and T is the temperature. While kinetic arguments are beyond the present model, here we will analyze the free energy of intermediates along possible catalytic pathways and discuss the effect of the applied potential and of the acid employed.

Reaction Pathways. With the set of linear free energy relationships, it is possible to build free energy landscapes with all of the possible catalytic intermediates. An example is given in Figure 7 for the H_2 production catalyst $[Ni(P^{Ph}{}_2N^{Ph}{}_2)_2]^{2+}$ (Ph = phenyl) with protonated dimethylformamide ($DMFH^+$, $pK_a = 6.1$)[62] as the external acid under 1 atm H_2 at the thermodynamic potential $E = E°(DMFH^+/DMF;H_2) = -0.386$ V,[61] and at the $E = E°_{II/I}(\mathbf{Ni^{2+}}) = -0.83$ V potential.[16] In these diagrams, the x-axis specifies the charge on the individual species (0, 1+, 2+, or 3+), and the y-axis specifies the number of hydrogen atoms bound to the complex regardless of their location (metal center or the pendant amines). For each charge and number of hydrogen atoms, possible isomers are grouped together.

Free energy landscapes such as those of Figure 7 can be used to construct free energy profiles for possible reaction pathways and make hypotheses on the catalytic mechanism (see also Supporting Information, Figure S6). For hydrogen production there are 6 different sequential electron (E) and proton (P) transfer reaction pathways, namely, EPEP (Electron−Proton−

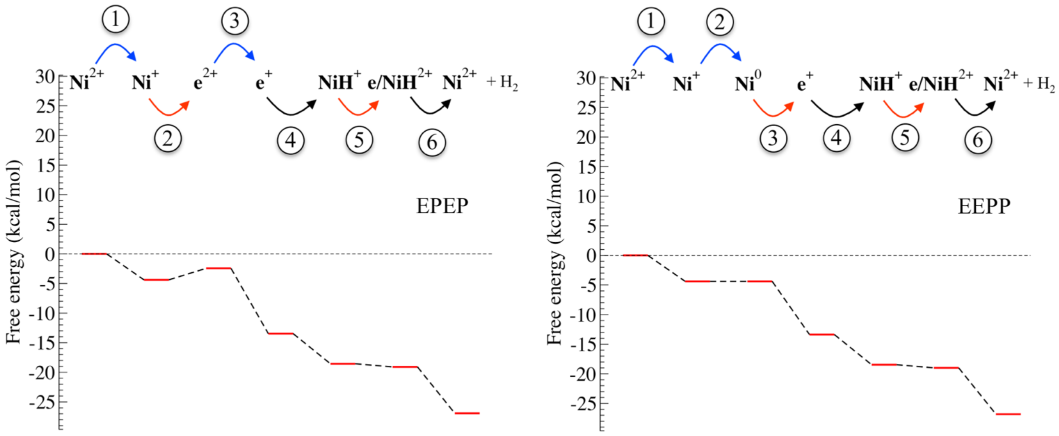

Figure 9. EPEP and EEPP reaction pathways for H_2 production from $DMFH^+$ ($pK_a = 6.1$) catalyzed by $[Ni(P^{Ph}{}_2N^{Ph}{}_2)_2]^{2+}$ at the applied potential $E = E°_{II/0}(\mathbf{Ni}^{+}) = -1.02$ V. Only endo protonation is considered. Blue arrow: electron transfer; red arrows: protonation step; black arrow: intramolecular proton movement.

Electron−Proton, the mechanism shown in Figure 2), EPPE, EEPP, PEPE, PEEP, and PPEE. The most favorable pathway should be the one that connects reactants to products by a series of energetically close intermediates. High or low energy intermediates are associated with high-energy barriers along the catalytic cycle and hence lead to inefficient catalysis.

Figure 7 (upper panel) shows that $\mathbf{Ni}^{2+}$ is the most stable species for $[Ni(P^{Ph}{}_2N^{Ph}{}_2)_2]^{2+}$ in $DMFH^+$ at $E = E°(DMFH^+/DMF;H_2)$ and 1 atm H_2. Protonation of $\mathbf{Ni}^{2+}$ to form $\mathbf{x}^{3+}$ ($pK_a^e(\mathbf{x}^{3+}) = 3.4$) or $\mathbf{e}^{3+}$ (Figure 7, step 1′, $pK_a^e(\mathbf{e}^{3+}) = 1.6$) is endothermic by +3.6 and +6.7 kcal/mol, respectively. Further protonation of $\mathbf{x}^{3+}$ or $\mathbf{e}^{3+}$ to yield $\mathbf{x/x}^{4+}$, $\mathbf{e/x}^{4+}$ or $\mathbf{e/e}^{4+}$ is even more endothermic and highly unfavorable. On the other hand, reduction of $\mathbf{e}^{3+}$ and $\mathbf{x}^{3+}$ species is endothermic at $E = E°(DMFH^+/DMF;H_2)$ leading to relatively high-energy $\mathbf{e}^{2+}$ and $\mathbf{x}^{2+}$ species (+11.2 and +9.3 kcal/mol above $\mathbf{Ni}^{2+}$). As discussed above, exo-protonated isomers are catalytically inefficient as they have to undergo multiple slow deprotonation/protonation steps to form the catalytically competent endo-protonated isomers, which result in low turnover frequencies (TOFs).[35] To keep the discussion simple, we will focus on endo protonation events only. Exo protonation is discussed in detail in the Supporting Information and to a lesser extent in the next section.

The pathways initiated by an initial electron transfer, as typified by the EPEP pathway (illustrated by solid arrows in Figure 7, steps 1 to 6) show that reduction of the $\mathbf{Ni}^{2+}$ species to $\mathbf{Ni}^{+}$ is also relatively high in energy (9.2 kcal/mol uphill, step 1). Protonation of $\mathbf{Ni}^{+}$ would result in slightly endothermic endo protonation (+1.9 kcal/mol, step 2). The resulting $\mathbf{e}^{2+}$ species can be readily reduced (+2.3 kcal/mol, step 3) to yield $\mathbf{e}^{+}$ that undergoes an intramolecular proton transfer to form the hydride $\mathbf{NiH}^{+}$ (−5.1 kcal/mol). The hydride, after an additional, slightly exothermic protonation provides an $\mathbf{e/NiH}^{2+}$ species, ultimately releases H_2 with an 8.1 kcal/mol exothermic step (experimental value 8.8 kcal/mol).[16] In Figure 7 (lower panel) we show how an applied potential of $E = E°_{II/I}(\mathbf{Ni}^{2+}) = -0.83$ V shifts the resulting relative free energies. The potential $E°_{II/I}(\mathbf{Ni}^{2+})$ is more negative than $E = E°(DMFH^+/DMF;H_2)$, and the difference in potential of about 0.44 V corresponds to the overpotential observed for this catalyst. Under these conditions the relative free energies of a number of species are negative, but the protonation steps are essentially unaffected and thus the PEPE, PEEP, and PPEE pathways remain uphill in energy, whereas the electron transfer steps along the EPEP pathway become essentially either energy neutral or downhill. These considerations suggest that H_2 evolution is initiated by an electron transfer step to form $\mathbf{Ni}^{+}$, ruling out PEPE, PEEP, and PPEE pathways, in agreement with the experimentally observed increased catalytic current at an applied potential of $E = E°_{II/I}(\mathbf{Ni}^{2+}) = -0.83$ V in acetonitrile.[16] Finally, it is stressed that these free energy landscapes provide us with the relative free energetics of all minima and hence all paths as well as potential undesired side reactions.

To extend this analysis by considering all six possible mechanisms for H_2 production, we use an alternate one-dimensional representation along the possible paths in Figure 8: note this representation removes species not directly involved along a given path and thus ultimately inhibits our ability to see potential side reactions. Consistent with the experimental evidence and theoretical mechanistic studies,[16,24] the EPEP process is the most favorable reaction pathway at −0.83 V. As indicated in Figure 8, protonation of reduced Ni species (EPEP, EPPE, and EEPP pathways) is more favorable than protonation of the Ni(II) complex (PEPE, PEEP, PPEE pathways). For an EEPP process, the $\mathbf{Ni}^{+}$ species must be reduced to $\mathbf{Ni}^{0}$. This second reduction step occurs at a potential of −1.02 V. As shown in Figure 9, at sufficiently negative applied potentials catalysis preferentially proceeds via the EEPP pathway as experimentally observed under several circumstances.

Protonation Sites and Effect of External Acid. Returning to our free energy map representation (Figure 7), we can readily gain important insights about the relative energetics of the various protonated species present in solution that may represent undesired reaction channels. Exo-protonated isomers are detrimental to catalysis. The possible branching in the catalytic cycle introduced by exo protonation are discussed in the Supporting Information (Section SI-4). Here we would like to stress that the ratio between endo and exo protonated species is critical to understand catalytic performances under steady state conditions. From Figure 7 it is evident that the relative stability of endo and exo depends on the oxidation state of the metal center. Singly endo-protonated Ni(0) isomers $\mathbf{e}^{+}$ are more stable than exo isomers $\mathbf{x}^{+}$, while the latter are always more stable for the Ni(I) and Ni(II) oxidation states. This observation can be generalized to any $[Ni(P^{R}{}_2N^{R'}{}_2)_2]^{2+}$ catalyst.

The distribution of doubly protonated isomers is more complex, and will be discussed in detail in Section 4.2.

For the current purposes it is important to recognize that the preferred catalytic pathway depends also on the acid employed as proton source. If the acid is strong enough, the pathways with protonation first can become favorable, as discussed in the next section. The employed acid not only determines the catalytic pathway, but most important, for a given catalyst, it determines the overpotential.

We now consider again H_2 evolution from $DMFH^+$ catalyzed by $[Ni(P^{Ph}{}_2N^{Ph}{}_2)_2]^{2+}$. Equation 11 gives an overpotential of 0.44 V at $E = E°_{II/I}(\mathbf{Ni^{2+}}) = -0.83$ V in agreement with the direct open circuit measuments.[16,61] To have zero overpotential for an EPEP process, an acid with a pK_a of 12.8 (eq 11) should be used. However, with such a weak acid it would be very difficult to protonate the pendant amines (11.1 kcal/mol uphill), as can be seen from the free energy profile of Figure 10 for an EPEP process with endo protonation only. The other possible pathways show similar high-energy protonated species for an external acid with a pK_a of 12.8. The overpotential can be reduced by using a more basic pendant amine such as that present in $[Ni(P^{Ph}{}_2N^{Bn}{}_2)_2]^{2+}$ (Bn = benzyl, see Supporting Information, Figure S6).[20] In this case the overpotential is less than 100 mV using 2-5-dichloroanilium (pK_a = 6.2), but the driving force for H_2 production is much lower and exo-protonation becomes preferred as will be discussed in the next section. Thus, a more basic pendant amine results in lower overpotential but also much lower rates.

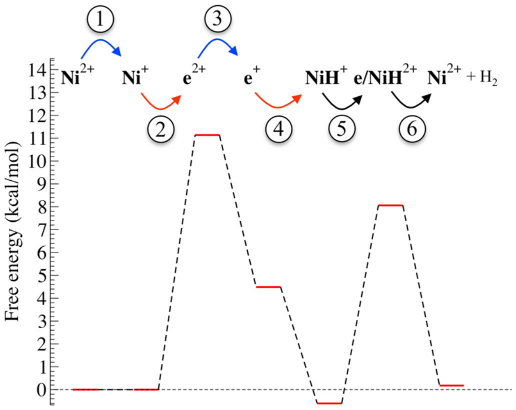

Figure 10. Free energy profile for H_2 production from an acid with pK_a = 12.8 catalyzed by $[Ni(P^{Ph}{}_2N^{Ph}{}_2)_2]^{2+}$ at the applied potential of $E = E°_{II/I}(\mathbf{Ni^{2+}}) = -0.83$ V according to an EPEP pathway Blue arrow: electron transfer; red arrows: protonation step; black arrow: intramolecular proton movement.

These last findings highlight a central issue often encountered in catalysis: changes in catalyst structure that make one step of a catalytic cycle more favorable often result in changes that make other steps less favorable. Importantly, the current analysis allows us to extract intimate details about these interconnections and offers a tool, which can allow us to postulate potential strategies around them. In this context it is critical to note that, the correlations presented in Section 3 allow us to estimate the influence of any structural modification on the entire free energy landscape for any reaction conditions for this class of compounds.

4.2. Distribution of Protonation Products. As discussed above, the possibility of protonating the pendant amines either endo or exo with respect to the metal center introduces branching along the catalytic cycle, disclosing pathways that are both kinetically and thermodynamically favored but that result in lower TOFs.[35,42] The linear free energy relationships derived in the present work allows us to map out the most stable doubly protonated intermediates for any $[Ni(P^{R}{}_2N^{R'}{}_2)_2]^{2+}$ system and the boundaries between them as a function of the reduction potential of the nonprotonated complex, $E°_{I/0}(\mathbf{Ni^+})$, and the pK_a of the parent aminium (Figure 11). These "isomer" diagrams are similar in spirit to structure maps commonly used in materials design,[63] but in contrast to these diagrams the current sets are expressed in terms of intrinsic thermodynamic properties of the $Ni(P_2N_2)_2$ complexes.

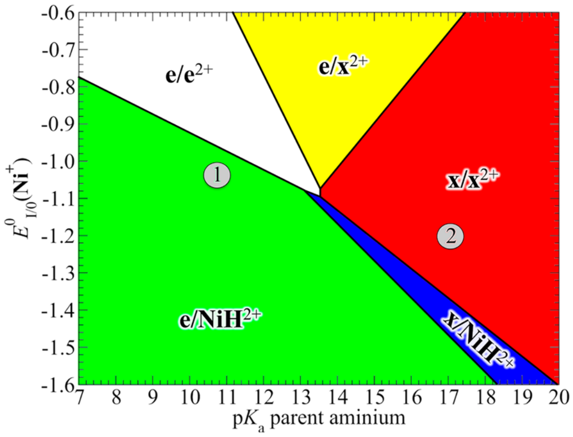

Figure 11. Distribution of lowest-free energy dicationic, doubly protonated isomers as a function of the Ni(I/0) redox potential, $E^0_{I/0}(\mathbf{Ni^{2+}})$, and the p$K_a$ of the parent aminium, pK_a($R'NH_3^+$). The two gray circles indicate the position of two catalysts for hydrogen production: (1) $[Ni(P^{Ph}{}_2N^{Ph}{}_2)_2]^{2+}$ and (2) $[Ni(P^{Ph}{}_2N^{Bn}{}_2)_2]^{2+}$.

Figure 11 shows that more negative $E^0_{I/0}(\mathbf{Ni^+})$ values (i.e., higher electron density on the Ni atom) favor the protonation at the metal center leading to the preferential formation of $\mathbf{e/NiH^{2+}}$ or $\mathbf{x/NiH^{2+}}$ over the $\mathbf{e/e^{2+}}$, $\mathbf{e/x^{2+}}$, and $\mathbf{x/x^{2+}}$ isomers. At the same time, more negative $E^0_{I/0}(\mathbf{Ni^+})$ values favor the formation Ni···H—N hydrogen bonds, which stabilize, if the pK_a of the parent aminium is low enough, the endo protonated $\mathbf{e/NiH^{2+}}$ and $\mathbf{e/e^{2+}}$ isomers. In contrast, for very basic pendant amines, the formation of strong N···H—N hydrogen bonds, which characterize the exo protonated complexes, leads to the formation $\mathbf{x/NiH^{2+}}$, $\mathbf{e/x^{2+}}$, or $\mathbf{x/x^{2+}}$ isomers depending on the $E^0_{I/0}(\mathbf{Ni^+})$ value. The catalytically competent endo protonated Ni(II) hydride, $\mathbf{e/NiH^{2+}}$, is the most stable doubly protonated species for the H_2 production catalyst $[Ni(P^{Ph}{}_2N^{Ph}{}_2)_2]^{2+}$ (point 1, Figure 11). For hydrogen production catalysts, $\mathbf{e/NiH^{2+}}$ is unstable toward the release of H_2 closing the catalytic cycle (see Figure 8). In contrast, the off-cycle exo doubly protonated species, $\mathbf{x/x^{2+}}$, is the most stable isomer for the $[Ni(P^{Ph}{}_2N^{Bn}{}_2)_2]^{2+}$ catalyst (point 2, Figure 11, see also Figure 2 and Supporting Information, Figure S6), which is a much slower but more energetically efficient (lower overpotential, see Section 4.1) catalyst for H_2 production. Further comments on the distribution of the protonation products are given in the Supporting Information (Section SI-7).

4.3. Pourbaix Diagrams. The knowledge of the free energy difference between species allows us to identify the most thermodynamically stable species of the $Ni(P^{R}{}_2N^{R'}{}_2)_2$ electrochemical system as a function of the applied potential and acidity of the solution, and to draw boundaries between them

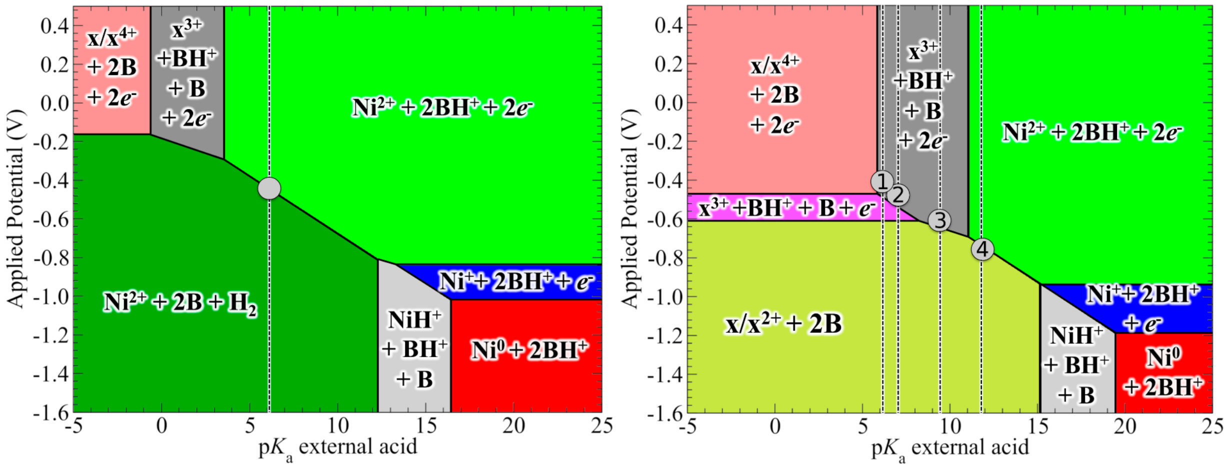

Figure 12. Pourbaix diagrams for the $[Ni(P^{Ph}{}_2N^{Ph}{}_2)_2]^{2+}$ (left panel) and $[Ni(P^{Ph}{}_2N^{Bn}{}_2)_2]^{2+}$ (right panel) complexes H_2 production catalysts. The vertical dashed lines indicate the pK_a values of acids used experimentally to test the catalytic activity of the two complexes. Left panel: protonated dimethylformamide, pK_a = 6.1. Right panel: 2–6-dichloroanilinium, pK_a = 5.1 (1); 2–5-dichloroanilium, pK_a = 6.2 (2); *p*-bromoanilinium, pK_a = 9.4 (3); *p*-anisidinium, pK_a = 11.8 (4).[48] The gray circles are located at the thermodynamic potential $E°(BH/B;H_2)$. The applied potential is relative to the ferrocenium/ferrocene couple.

(Pourbaix diagrams).[14,37] Although these diagrams do not provide any information about the kinetics of the catalytic reaction, they still provide useful information on the catalytic mechanism. As an example, in Figure 12 the Pourbaix diagrams for the H_2 production catalysts $[Ni(P^{Ph}{}_2N^{Ph}{}_2)_2]^{2+}$ and $[Ni(P^{Ph}{}_2N^{Bn}{}_2)_2]^{2+}$ are reported. In the case of the $[Ni(P^{Ph}{}_2N^{Ph}{}_2)_2]^{2+}$ complex, the most stable species in the presence of an external acid with a pK_a > 3.2 is the nonprotonated Ni(II) complex. Therefore, when acids with pK_a values between 3.2 and 6.5 are used for H_2 production, $[Ni(P^{Ph}{}_2N^{Ph}{}_2)_2]^{2+}$ is first reduced and then protonated. In contrast, for $[Ni(P^{Ph}{}_2N^{Bn}{}_2)_2]^{2+}$ exo singly, $\mathbf{x}^{3+}$, and doubly protonated, $\mathbf{x/x}^{4+}$, Ni(II) species are expected in the presence of acids with a pK_a as high as 11, and for this catalyst the first reduction step is expected to occur after one or two protonation steps depending on the strength of the acid (see Supporting Information, Figure S6). These observations are consistent with the experimental evidence.[20,37] Most importantly, the Pourbaix diagrams for these two systems reveal that the most stable species under the applied potentials (invariably more negative than the thermodynamic potential) and acid strengths that have been used for studying catalysis are the nonprotonated Ni(II) species, $\mathbf{Ni}^{2+}$, and the doubly exo protonated, $\mathbf{x/x}^{2+}$, isomer for $[Ni(P^{Ph}{}_2N^{Ph}{}_2)_2]^{2+}$ and $[Ni(P^{Ph}{}_2N^{Bn}{}_2)_2]^{2+}$, respectively. As discussed in the introduction, only the $\mathbf{e/NiH}^{2+}$ is catalytically active for the formation of H_2.[35,42] This species, which is the most stable doubly protonated species for the $[Ni(P^{Ph}{}_2N^{Ph}{}_2)_2]^{2+}$ complex, is unstable toward the release of H_2 (Figure 11). In contrast, for the $[Ni(P^{Ph}{}_2N^{Bn}{}_2)_2]^{2+}$ complex, the exo doubly protonated $\mathbf{x/x}^{2+}$ isomer is the most stable species under catalytic conditions. This is consistent with the far lower TOF observed for this catalyst compared to $[Ni(P^{Ph}{}_2N^{Ph}{}_2)_2]^{2+}$ (TOF < 0.5 s^{-1} and 320 s^{-1} for $[Ni(P^{Ph}{}_2N^{Bn}{}_2)_2]^{2+}$ and $[Ni(P^{Ph}{}_2N^{Ph}{}_2)_2]^{2+}$).[16,17,20] However, the $[Ni(P^{Ph}{}_2N^{Bn}{}_2)_2]^{2+}$ catalyst[20,37] is energetically more efficient and operates at a lower overpotential than the $[Ni(P^{Ph}{}_2N^{Ph}{}_2)_2]^{2+}$ catalyst, consistent with our observation above about the influence of exo protonation on the redox couple. Finally it is noted that with our current set of equations it is now possible to automatically generate a Pourbaix diagram for any catalyst in this family a priori.

5. CONCLUSIONS

We have outlined an approach for organizing and using quantitative thermodynamic information of potential catalytic intermediates as a powerful tool for rational design of molecular catalysts. This work provides a paradigm for rapidly assessing and understanding potential catalytic bottlenecks, side reactions, and the interconnection between structural modification and catalyst performance. We have illustrated the strength and potential of this approach by focusing on $[Ni(P^{R}{}_2N^{R'}{}_2)_2]^{2+}$ catalysts for H_2 oxidation/production.

We first constructed a set of linear free energy relationships, based on an extensive series of electronic structure calculations, for predicting the thermodynamic properties of intermediates involved in the catalytic oxidation and production of H_2 using $[Ni(P^{R}{}_2N^{R'}{}_2)_2]^{2+}$ catalysts. These thermodynamic properties include reduction potentials, hydride donor abilities, and pK_a values. The proposed correlations require the knowledge of the two redox potentials for the Ni(II)/Ni(I) and Ni(I)/Ni(0) couples of nonprotonated complexes, $E°_{II/I}(\mathbf{Ni}^{2+})$ and $E°_{I/0}(\mathbf{Ni}^{+})$, and p$K_a$ of the parent aminium, p$K_a(R'NH_3{}^+)$. These three quantities are readily available or easily accessible either experimentally or theoretically. It is remarkable that the majority of the properties can be predicted with the knowledge of only $E°_{I/0}(\mathbf{Ni}^{+})$ and p$K_a(R'NH_3{}^+)$.

As a second step, we used the derived linear free energy relationships to build free energy maps such as those reported in Figure 7 for any $[Ni(P^{R}{}_2N^{R'}{}_2)_2]^{2+}$ under any applied potential and external base (H_2 oxidation) or acid (H_2 production). This information permits a systematic search for testing hypotheses when searching for optimal catalysts and optimal catalytic conditions. One then looks for paths that avoid high-energy species, which are associated with high activation barriers, and low-energy species, which represent thermodynamic sinks. These relationships allow one to make testable hypotheses based on the characteristics sought for an ideal catalyst. Our approach also gives some insights about potential side reactions that could be detrimental to catalyst performance, which we have illustrated with a discussion on how to optimize some of the critical steps (protonation and deprotonation of the pendant amines) to favor the catalytically competent endo protonated intermediates such as **e**/**e**$^{2+}$ and **e**/**NiH**$^{2+}$ species, with particular focus on reducing the overpotential of H_2 production.

Our findings highlight the central challenge whereby changes in catalyst structure that make one step of a catalytic cycle more favorable often result in changes that make another step less favorable. This leads naturally to the question of how we can optimize catalysts to improve their overall performance. We believe a detailed and comprehensive thermodynamic analysis as provided here can serve as a first, powerful step in such an evaluation. Our approach can be generalized into three steps: (1) Validate theoretical protocols against existing thermodynamic data for validation and verification. (2) Construct correlations between thermodynamic properties to predict relative free energies of all intermediates in the catalytic process. (3) Employ free landscapes to follow the trends and interconnections between the energetics of these intermediates. This approach is in principle extensible to any class of catalyst, as it relies on well-proven concepts, such as linear free energy relationships, which have been validated for a large number of catalytic systems. The approach is, however, limited by the fact that it does not account for kinetic barriers, which may make some thermodynamically accessible minima kinetically inaccessible, but (if done correctly) will identify potential high- or low-energy intermediates that should be avoided. Finally, efforts toward the design of new catalysts with high turnover rates and low overpotentials are underway in our laboratory by incorporating these free energy relationships into an equally comprehensive microkinetic model for prediction of the trends in catalytic activity.

■ ASSOCIATED CONTENT

Ⓢ Supporting Information

(1) List of all of the species considered in present work; (2) extended thermodynamics map, which includes the possibility of exo protonation; (3) discussion on the isodesmic scheme used for the evaluation of the thermodynamics properties; (4) analysis of the influence of the coordinated acetonitrile solvent molecule on the redox properties of the Ni(II) complexes; (5) additional comments on the linear correlations for the acidity of the pendant aminiums; (6) comparison of measured and calculated thermodynamic quantities; (7) further comments on protonation pathways and the distribution of protonation products; (8) optimized Cartesian coordinates of all of the species considered in the present work. This material is available free of charge via the Internet at http://pubs.acs.org.

■ AUTHOR INFORMATION

Corresponding Authors

*E-mail: roger.rousseau@pnnl.gov (R.R.).
*E-mail: simone.raugei@pnnl.gov (S.R.).

Notes

The authors declare no competing financial interest.

■ ACKNOWLEDGMENTS

We thank Dr. Aaron Appel, Dr. Eric Wiedner, and Dr. Monte Helm for stimulating discussions. This research was supported as part of the Center for Molecular Electrocatalysis, an Energy Frontier Research Center funded by the U.S. Department of Energy, Office of Science, Office of Basic Energy Sciences. Computational resources were provided at W. R. Wiley Environmental Molecular Science Laboratory at Pacific Northwest National Laboratory) and the National Energy Research Scientific Computing Center (NERSC) at Lawrence Berkeley National Laboratory.

■ REFERENCES

(1) Friedman, D.; Masciangioli, T.; Olson, S. *The Role of the Chemical Sciences in Finding Alternatives to Critical Resources: A Workshop Summary*; National Academies Press: Washington, DC, 2012.

(2) Bullock, R. M., Ed.; *Catalysis without Precious Metals*; Wiley-VCH: Weinheim, Germany, 2010.

(3) Lewis, N. S.; Nocera, D. G. *Proc. Natl. Acad. Sci. U.S.A.* **2006**, *103*, 15729−15735.

(4) Cook, T. R.; Dogutan, D. K.; Reece, S. Y.; Surendranath, Y.; Teets, T. S.; Nocera, D. G. *Chem. Rev.* **2010**, *110*, 6474−6502.

(5) Tran, P. D.; Artero, V.; Fontecave, M. *Energy Environ. Sci.* **2010**, *3*, 727−747.

(6) Jeletic, M. S.; Mock, M. T.; Appel, A. M.; Linehan, J. C. *J. Am. Chem. Soc.* **2013**, *135*, 11533−11536.

(7) Rakowski DuBois, M.; DuBois, D. L. *Chem. Soc. Rev.* **2009**, *38*, 62−72.

(8) DuBois, D. L.; Bullock, R. M. *Eur. J. Inorg. Chem.* **2011**, *2011*, 1017−1027.

(9) Mock, M. T.; Potter, R. G.; Camaioni, D. M.; Li, J.; Dougherty, W. G.; Kassel, W. S.; Twamley, B.; DuBois, D. L. *J. Am. Chem. Soc.* **2009**, *131*, 14454−14465.

(10) Mock, M. T.; Potter, R. G.; O'Hagan, M. J.; Camaioni, D. M.; Dougherty, W. G.; Kassel, W. S.; DuBois, D. L. *Inorg. Chem.* **2011**, *50*, 11914−11928.

(11) DuBois, D. L.; Blake, D. M.; Miedaner, A.; Curtis, C. J.; DuBois, M. R.; Franz, J. A.; Linehan, J. C. *Organometallics* **2006**, *25*, 4414−4419.

(12) Ellis, W. W.; Miedaner, A.; Curtis, C. J.; Gibson, D. H.; DuBois, D. L. *J. Am. Chem. Soc.* **2002**, *124*, 1926−1932.

(13) Fraze, K.; Wilson, A. D.; Appel, A. M.; Rakowski DuBois, M.; DuBois, D. L. *Organometallics* **2007**, *26*, 3918−3924.

(14) Small, Y. A.; DuBois, D. L.; Fujita, E.; Muckerman, J. T. *Energy Environ. Sci.* **2011**, *4*, 3008−3020.

(15) Wilson, A. D.; Shoemaker, R. K.; Miedaner, A.; Muckerman, J. T.; DuBois, D. L.; DuBois, M. R. *Proc. Natl. Acad. Sci. U.S.A.* **2007**, *104*, 6951−6956.

(16) Kilgore, U. J.; Roberts, J. A. S.; Pool, D. H.; Appel, A. M.; Stewart, M. P.; DuBois, M. R.; Dougherty, W. G.; Kassel, W. S.; Bullock, R. M.; DuBois, D. L. *J. Am. Chem. Soc.* **2011**, *133*, 5861−5872.

(17) Kilgore, U. J.; Stewart, M. P.; Helm, M. L.; Dougherty, W. G.; Kassel, W. S.; DuBois, M. R.; DuBois, D. L.; Bullock, R. M. *Inorg. Chem.* **2011**, *50*, 10908−10918.

(18) Wiese, S.; Kilgore, U. J.; DuBois, D. L.; Bullock, R. M. *ACS Catal.* **2012**, *2*, 720−727.

(19) Yang, J. Y.; Chen, S.; Dougherty, W. G.; Kassel, W. S.; Bullock, R. M.; DuBois, D. L.; Raugei, S.; Rousseau, R.; Dupuis, M.; DuBois, M. R. *Chem. Commun.* **2010**, *46*, 8618−8620.

(20) Appel, A. M.; Pool, D. H.; O'Hagan, M.; Shaw, W. J.; Yang, J. Y.; Rakowski DuBois, M.; DuBois, D. L.; Bullock, R. M. *ACS Catal.* **2011**, *1*, 777−785.

(21) Yang, J. Y.; Smith, S. E.; Liu, T.; Dougherty, W. G.; Hoffert, W. A.; Kassel, W. S.; Rakowski DuBois, M.; DuBois, D. L.; Bullock, R. M. *J. Am. Chem. Soc.* **2013**, *135*, 9700−9712.

(22) Chen, S.; Rousseau, R.; Raugei, S.; Dupuis, M.; DuBois, D. L.; Bullock, R. M. *Organometallics* **2011**, *30*, 6108−6118.

(23) Chen, S.; Raugei, S.; Rousseau, R.; Dupuis, M.; Bullock, R. M. *J. Phys. Chem. A* **2010**, *114*, 12716−12724.

(24) Raugei, S.; Chen, S.; Ho, M.-H.; Ginovska-Pangovska, B.; Rousseau, R. J.; Dupuis, M.; DuBois, D. L.; Bullock, R. M. *Chem.—Eur. J.* **2012**, *18*, 6493−6506.

(25) Dupuis, M.; Chen, S.; Raugei, S.; DuBois, D. L.; Bullock, R. M. *J. Phys. Chem. A* **2011**, *115*, 4861−4865.

(26) Barton, B. E.; Olsen, M. T.; Rauchfuss, T. B. *J. Am. Chem. Soc.* **2008**, *130*, 16834−16835.

(27) Carroll, M. E.; Barton, B. E.; Rauchfuss, T. B.; Carroll, P. J. *J. Am. Chem. Soc.* **2012**, *134*, 18843−18852.
(28) Singleton, M. L.; Crouthers, D. J.; Duttweiler, R. P.; Reibenspies, J. H.; Darensbourg, M. Y. *Inorg. Chem.* **2011**, *50*, 5015−5026.
(29) Jiang, S.; Liu, J.; Shi, Y.; Wang, Z.; Åkermark, B.; Sun, L. *Dalton Trans.* **2007**, 896−902.
(30) Kaur-Ghumaan, S.; Schwartz, L.; Lomoth, R.; Stein, M.; Ott, S. *Angew. Chem., Int. Ed.* **2010**, *49*, 8033−8036.
(31) Lounissi, S.; Zampella, G.; Capon, J.-F.; De Gioia, L.; Matoussi, F.; Mahfoudhi, S.; Pétillon, F. Y.; Schollhammer, P.; Talarmin, J. *Chem.—Eur. J.* **2012**, *18*, 11123−11138.
(32) Camara, J. M.; Rauchfuss, T. B. *Nat. Chem.* **2012**, *4*, 26−30.
(33) Wang, N.; Wang, M.; Wang, Y.; Zheng, D.; Han, H.; Ahlquist, M. S. G.; Sun, L. *J. Am. Chem. Soc.* **2013**, *135*, 13688−13691.
(34) Liu, T.; DuBois, D. L.; Bullock, R. M. *Nat. Chem.* **2013**, *5*, 228−233.
(35) O'Hagan, M.; Ho, M.-H.; Yang, J. Y.; Appel, A. M.; DuBois, M. R.; Raugei, S.; Shaw, W. J.; DuBois, D. L.; Bullock, R. M. *J. Am. Chem. Soc.* **2012**, *134*, 19409−19424.
(36) O'Hagan, M.; Shaw, W. J.; Raugei, S.; Chen, S.; Yang, J. Y.; Kilgore, U. J.; DuBois, D. L.; Bullock, R. M. *J. Am. Chem. Soc.* **2011**, *133*, 14301−14312.
(37) Horvath, S.; Fernandez, L. E.; Appel, A. M.; Hammes-Schiffer, S. *Inorg. Chem.* **2013**, *52*, 3643−3652.
(38) Horvath, S.; Fernandez, L. E.; Soudackov, A. V.; Hammes-Schiffer, S. *Proc. Natl. Acad. Sci. U.S.A.* **2012**, *109*, 15663−15668.
(39) Fernandez, L. E.; Horvath, S.; Hammes-Schiffer, S. *J. Phys. Chem. Lett.* **2013**, *4*, 542−546.
(40) Fernandez, L. E.; Horvath, S.; Hammes-Schiffer, S. *J. Phys. Chem. C* **2012**, *116*, 3171−3180.
(41) Carver, C. T.; Matson, B. D.; Mayer, J. M. *J. Am. Chem. Soc.* **2012**, *134*, 5444−5447.
(42) Stewart, M. P.; Ho, M.-H.; Wiese, S.; Lindstrom, M. L.; Thogerson, C. E.; Raugei, S.; Bullock, R. M.; Helm, M. L. *J. Am. Chem. Soc.* **2013**, *135*, 6033−6046.
(43) Wayner, D. D. M.; Parker, V. D. *Acc. Chem. Res.* **1993**, *26*, 287−294.
(44) Appel, A. M.; Lee, S.-J.; Franz, J. A.; DuBois, D. L.; Rakowski DuBois, M.; Twamley, B. *Organometallics* **2009**, *28*, 749−754.
(45) Yang, J. Y.; Bullock, R. M.; Shaw, W. J.; Twamley, B.; Fraze, K.; DuBois, M. R.; DuBois, D. L. *J. Am. Chem. Soc.* **2009**, *131*, 5935−5945.
(46) Qi, X.-J.; Fu, Y.; Liu, L.; Guo, Q.-X. *Organometallics* **2007**, *26*, 4197−4203.
(47) Qi, X.-J.; Liu, L.; Fu, Y.; Guo, Q.-X. *Organometallics* **2006**, *25*, 5879−5886.
(48) Kaljurand, I.; Kütt, A.; Sooväli, L.; Rodima, T.; Mäemets, V.; Leito, I.; Koppel, I. A. *J. Org. Chem.* **2005**, *70*, 1019−1028.
(49) Perdew, J. P. *Phys. Rev. B* **1986**, *33*, 8822−8824.
(50) Perdew, J. P. *Phys. Rev. B* **1986**, *34*, 7406−7406.
(51) Becke, A. D. *Phys. Rev.* **1988**, *38*, 3098−3100.
(52) Andrae, D.; Häußermann, U.; Dolg, M.; Stoll, H.; Preuß, H. *Theor. Chim. Acta* **1990**, *77*, 123−141.
(53) Rassolov, V. A.; Pople, J. A.; Ratner, M. A.; Windus, T. L. *J. Chem. Phys.* **1998**, *109*, 1223.
(54) Barone, V.; Cossi, M. *J. Phys. Chem. A* **1998**, *102*, 1995−2001.
(55) Cossi, M.; Rega, N.; Scalmani, G.; Barone, V. *J. Comput. Chem.* **2003**, *24*, 669−681.
(56) Bondi, A. *J. Phys. Chem.* **1964**, *68*, 441−451.
(57) Frisch, M. J.; Trucks, G. W.; Schlegel, H. B.; Scuseria, G. E.; Robb, M. A.; Cheeseman, J. R.; Scalmani, G.; Barone, V.; Mennucci, B.; Petersson, G. A.; Nakatsuji, H.; Caricato, M.; Li, X.; Hratchian, H. P.; Izmaylov, A. F.; Bloino, J.; Zheng, G.; Sonnenberg, J. L.; Hada, M.; Ehara, M.; Toyota, K.; Fukuda, R.; Hasegawa, J.; Ishida, M.; Nakajima, T.; Honda, Y.; Kitao, O.; Nakai, H.; Vreven, T.; Montgomery, Jr., J. A.; Peralta, J. E.; Ogliaro, F.; Bearpark, M.; Heyd, J. J.; Brothers, E.; Kudin, K. N.; Staroverov, V. N.; Kobayashi, R.; Normand, J.; Raghavachari, K.; Rendell, A.; Burant, J. C.; Iyengar, S. S.; Tomasi, J.; Cossi, M.; Rega, N.; Millam, N. J.; Klene, M.; Knox, J. E.; Cross, J. B.; Bakken, V.; Adamo, C.; Jaramillo, J.; Gomperts, R.; Stratmann, R. E.; Yazyev, O.; Austin, A. J.; Cammi, R.; Pomelli, C.; Ochterski, J. W.; Martin, R. L.; Morokuma, K.; Zakrzewski, V. G.; Voth, G. A.; Salvador, P.; Dannenberg, J. J.; Dapprich, S.; Daniels, A. D.; Farkas, O.; Foresman, J. B.; Ortiz, J. V.; Cioslowski, J.; Fox, D. J. *Gaussian 09*, Revision A.1; Gaussian, Inc.: Wallingford, CT, 2009.
(58) Nørskov, J. K.; Rossmeisl, J.; Logadottir, A.; Lindqvist, L.; Kitchin, J. R.; Bligaard, T.; Jónsson, H. *J. Phys. Chem. B* **2004**, *108*, 17886−17892.
(59) Wiedner, E. S.; Yang, J. Y.; Chen, S.; Raugei, S.; Dougherty, W. G.; Kassel, W. S.; Helm, M. L.; Bullock, R. M.; DuBois, M. R.; DuBois, D. L. *Organometallics* **2012**, *31*, 144−156.
(60) Savéant, J.-M. *Chem. Rev.* **2008**, *108*, 2348−2378.
(61) Roberts, J. A. S.; Bullock, R. M. *Inorg. Chem.* **2013**, *52*, 3823−3835.
(62) Kolthoff, I. M.; Chantooni, M. K.; Bhowmik, S. *Anal. Chem.* **1967**, *39*, 1627−1633.
(63) Pettifor, D. G. *Bonding and Structure of Molecules and Solids*; Oxford University Press: Oxford, U.K., 1995.

■ NOTE ADDED AFTER ASAP PUBLICATION

This paper was published ASAP December 16, 2013. Corrections were made to the SI and the paper reposted on December 18, 2013.